Connection of Surface Snowfall Bias to Cloud Phase Bias - Satellite Observations, ERA5, and CMIP6

Franziska Hellmuth[1], Tim Carlsen[1], Anne Sophie Daloz[2], Robert Oscar David[1], and Trude Storelvmo[1]

[1]Department of Geosciences, University of Oslo, Blindernveien 31, 0371, Oslo, Norway
[2]Center for International Climate Research (CICERO), Gaustadalleen 21, 0349, Oslo, Norway

Correspondence: Franziska Hellmuth (franziska.hellmuth@geo.uio.no)

Abstract. Supercooled Liquid-Containing Clouds (sLCCs) play a significant role in Earth's radiative budget and the hydrological cycle, especially through surface snowfall production. Evaluating state-of-the-art climate models with respect to their ability to simulate the frequency of occurrence of sLCCs and the frequency with which they produce snow is, therefore, critically important. Here, we compare these quantities as derived from satellite observations, reanalysis datasets, and Earth System Models from Phase 6 of the Coupled Model Intercomparison Project (CMIP6) and find significant discrepancies between the data sets for mid and high latitudes in both hemispheres. Specifically, we find that the ERA5 reanalysis and ten CMIP6 models consistently overestimate the frequency of sLCCs and snowfall frequencies from sLCCs compared to CloudSat-CALIPSO satellite observations, especially over open ocean regions. The biases are very similar for ERA5 and the CMIP6 models, which indicates that the discrepancies in cloud phase and snowfall stem from differences in the representation of cloud microphysics rather than the representation of meteorological conditions. This, in turn, highlights the need for refinements in the models' parameterizations of cloud microphysics in order for them to represent cloud phase and snowfall accurately. The thermodynamic phase of clouds and precipitation has a strong influence on simulated climate feedbacks and, thus, projections of future climate. Understanding the origin(s) of the biases identified here is, therefore, crucial for improving the overall reliability of climate models.

1 Introduction

The importance of snowfall and snow cover cannot be overestimated, as they affect the Earth's energy budget and the hydrological cycle, especially in mid- and high-latitudes, and thereby strongly influence ecosystems and human societies in these regions. Snowfall is also an important water resource globally (Barnett et al., 2005). At the same time, heavy snowfall events have the potential to negatively impact local communities and infrastructure (Eisenberg and Warner, 2005; Scott et al., 2008; Fox et al., 2023). Snow cover plays an important role for Earth's radiative properties through its effect on surface albedo by reducing the absorption of solar energy (Zhang, 2005).

Snowfall is directly linked to the cloud phase, as it can originate from pure ice clouds as well as supercooled liquid-containing clouds (sLCCs), where both supercooled water droplets and ice crystals coexist at temperatures between $-40°C$ and $0°C$ (Jiusto and Weickmann, 1973; Korolev et al., 2017). These sLCCs dominate at latitudes higher than $45°$ and cover up to

25 20% − 30% of the Earth depending on the season (Warren et al., 1988; Matus and L'Ecuyer, 2017). Clouds reflect solar radiation (cooling the surface) and trap terrestrial radiation (warming the surface). The balance between the two effects is, among others, influenced by the phase composition of the clouds due to distinct scattering properties of liquid and ice (Shupe and Intrieri, 2004; Ehrlich et al., 2009; Cesana et al., 2012). For otherwise similar properties, a cloud with more liquid reflects more solar radiation back to space. Therefore, representing the cloud phase correctly in Earth System Models (ESMs) has
30 substantial implications for the simulation of cloud radiative properties (Matus and L'Ecuyer, 2017), especially in future climate projections with a warmer climate. This represents an important component of the cloud feedback, i.e., how clouds respond to changes in surface air temperature and how these changes, in turn, influence temperature. The cloud feedback is, at present, the most uncertain physical climate feedback, significantly contributing to the spread of climate sensitivity in ESMs (Zelinka et al., 2020). Among the most poorly understood cloud feedbacks is the one associated with cloud phase changes (Bjordal
35 et al., 2020; Zelinka et al., 2020).

Atmospheric warming can lead to cloud phase changes through two different pathways: less cloud ice due to higher temperatures or more ice due to potentially more ice-nucleating particles (INPs). INPs are microscopic particles present in the air that serve as the starting point of ice crystal formation in clouds (DeMott et al., 2010). Several studies, including Murray et al. (2021) showed that increased temperatures, especially in polar regions, have caused a shift of mixed-phase clouds towards
40 higher latitudes and altitudes due to the ice reduction in the atmosphere in these regions. The shift in cloud phase towards more liquid and less ice leads to a reduction in the fraction of precipitation falling as snow, resulting in an expected decrease in snowfall events and duration of the snowfall season for most regions in the Northern Hemisphere (NH, Danco et al., 2016; Chen et al., 2020). However, potentially partly counteracting this, the reduction in Arctic sea ice may also facilitate local emission of INPs (Carlsen and David, 2022). Furthermore, the well-established general increase in total precipitation with warming
45 may also lead to increased snowfall in some regions (Douville et al., 2023). Hence, cloud phase, snowfall amounts, and snowfall frequency of occurrence will likely change with warming in ways that are both complex and currently poorly understood (Danco et al., 2016; Chen et al., 2020; Quante et al., 2021).

There are several processes governing snow formation within sLCCs. The transition from a fully liquid to a completely frozen cloud can follow various pathways (Costa et al., 2017), driven by differences in saturation vapor pressures of ice and
50 liquid at temperatures below 0°C (Wegener, 1912; Bergeron, 1928; Findeisen, 2015), where ice crystals will grow at the expense of supercooled liquid water (Korolev and Mazin, 2003; Korolev, 2007; Storelvmo and Tan, 2015; Korolev et al., 2017). This phenomenon is called the Wegener-Bergeron-Findeisen (WBF) process and can lead to the rapid growth of ice crystals, which eventually fall out as snow. Increasing INP concentrations can cause cloud glaciation, amplified by the WBF process, increasing the precipitation at the surface and consequently shortening the cloud lifetime (Lohmann and Diehl, 2006;
55 Rosenfeld et al., 2011; Storelvmo and Tan, 2015). Furthermore, ice crystals can be introduced into this sLCC by either falling into it from above (e.g. Proske et al., 2021) or by turbulent mixing.

The microphysical processes described above occur on scales smaller than the grid resolution used in ESMs and their influence on cloud macroscopic properties must therefore be parameterized. Cloud microphysical parameterizations in ESMs are known to often be overly crude and simplistic. For example, ESMs generally assume that liquid and ice are uniformly

60   mixed within a grid box, while observations have shown that sLCCs typically consist of cloud pockets exclusively composed of liquid or ice (Korolev and Milbrandt, 2022). Additionally, the treatment of primary ice production has an influence on the amount of supercooled liquid water in climate models (Vergara-Temprado et al., 2018). Only a small number of ESMs include parameterizations of primary ice production that depend on the presence of aerosols with the ability to act as INPs, while the majority include simpler parameterizations that rely only on temperature. Cesana et al. (2015) found that models with

65   more complex microphysics (e.g., prognostic ice and liquid water content, heterogeneous freezing, riming, accretion, and the WBF process) tend to provide a more accurate representation of the ice phase. Similarly, Komurcu et al. (2014) noted that the variability in cloud phase among models was influenced by the specific ice nucleation scheme used and the representation of other microphysical processes associated with ice.

ESMs have previously been shown to not accurately represent cloud phase by often underestimating liquid and overestimat-

70   ing ice, compared to satellite measurements (Komurcu et al., 2014; Cesana et al., 2015; Tan and Storelvmo, 2016; Kay et al., 2016; McIlhattan et al., 2017; Bruno et al., 2021; Shaw et al., 2022). However, most studies to date were conducted based on the previous generation of ESMs (Coupled Model Intercomparison Project 5 (CMIP5), Taylor et al., 2012), and a wide range of different cloud phase metrics have been applied in the past, often without a clear strategy that allows like-for-like comparison with satellite observations. In other words, uncertainties remain in understanding the complex processes governing

75   cloud phase and their representation in ESMs (Komurcu et al., 2014). Because cloud phase and snowfall are tightly linked through the processes outlined earlier, any inaccuracies in representing cloud phase must lead to biases in the simulation of snow growth, formation, and the precipitation reaching the ground in solid or liquid form (Mülmenstädt et al., 2021; Stanford et al., 2023).

CloudSat (Stephens et al., 2002) and Cloud-Aerosol Lidar and Infrared Pathfinder Satellite Observation (CALIPSO, Winker

80   et al., 2010), flying in the afternoon-train constellation, provide global estimates of cloud properties and snowfall since 2006. CloudSat is equipped with a Cloud Profiling Radar (CPR) that detects large cloud and precipitation particles, while CALIPSO with its Cloud-Aerosol Lidar with Orthogonal Polarization (CALIOP, Winker et al., 2007), can among other things, determine the phase of cloud layers. The CloudSat-CALIPSO constellation overpasses the same regions approximately every 16 days, allowing for continuous monitoring of cloud and snowfall characteristics. Previous studies have contributed to a better under-

85   standing of the uncertainties associated with satellite measurements of clouds and precipitation (e.g., Stephens and Kummerow, 2007; Hiley et al., 2011). Despite limitations, the value of satellite data like CloudSat and CALIPSO for validating reanalysis and ESM data, which both rely on parameterized microphysics (Forbes and Ahlgrimm, 2014; McIlhattan et al., 2017; Milani et al., 2018; Edel et al., 2020; Daloz et al., 2020) is well established. Previous studies have shown that ESMs produce double the amount of snowfall relative to satellite observations (Heymsfield et al., 2020). Additionally, Roussel et al. (2020) discov-

90   ered that the ensemble median of CMIP5 experiments tend to show a positive bias in snowfall rates compared to the CloudSat average. Of particular relevance for the analysis presented here is the study by McIlhattan et al. (2017), who investigated the causes and impacts of liquid-containing cloud (LCC) biases in the Arctic region. They found that the Community Earth System Model Large Ensemble (CESM-LE) underestimates the frequency of Arctic LCCs compared to observations. Moreover, the CESM-LE overestimated the snowfall frequency from these clouds, possibly indicating an overactive WBF process leading to

95   too frequent snowfall and too short cloud lifetime (McIlhattan et al., 2017). In a comparable study of the Southern Hemisphere
(SH), Roussel et al. (2020) showed a weak annual cycle of snowfall rates in the Antarctic plateau regions and found that the
CMIP5 and CMIP6 (Eyring et al., 2016) simulations tended to overestimate the average precipitation rate in Antarctica. Despite
the improvements in surface temperature representation from CMIP5 to CMIP6, there is no corresponding improvement in the
representation of large-scale mean precipitation rate and seasonality in the region (Roussel et al., 2020). Precipitation errors

100   in ESMs are not primarily driven by first-order physical links but by atmospheric circulation and cloud microphysics (Roussel
et al., 2020). Antarctica and the surrounding ocean are also known to be a region in which ESMs have large biases, which are
thought to be attributable to cloud phase biases (e.g. Vergara-Temprado et al., 2018). These persistent discrepancies between
ESMs and observations further highlight the importance of understanding the link between cloud phase and solid precipitation
on different scales and improving the representation of cloud phase in ESMs.

105   Reanalysis products employ numerical weather prediction models that assimilate various observations to generate a contin-
uous spatial and temporal dataset. The European Center for Medium-Range Weather Forecasts (ECMWF) reanalysis datasets
use data collected from satellites, weather stations, and ocean buoys to combine with a numerical weather prediction model
to provide a comprehensive view of the global atmospheric climate. Nonetheless, the precision in depicting cloud and surface
snowfall relies on the underlying model and the assimilated dataset (Boisvert et al., 2018; Daloz et al., 2020; Boisvert et al.,

110   2020). Challenges may arise due to limited spatial resolution and sparse observations, particularly in remote and complex to-
pographical regions (Boisvert et al., 2018; Daloz et al., 2020; Boisvert et al., 2020). Wang et al. (2019) studied snowfall within
two ECMWF reanalysis data sets, ERA-Interim (Simmons et al., 2007; Dee et al., 2011) and ERA5 (Hersbach et al., 2020).
The latter includes higher horizontal resolution, improvements to the numerical model, improved data assimilation, and differ-
ent cloud physics schemes (Forbes and Ahlgrimm, 2014). Wang et al. (2019) showed that ERA5 led to a better representation

115   of snowfall than ERA-Interim. Nevertheless, Milani et al. (2018) concluded that ERA-Interim reanalysis data produce mean
annual snowfall patterns similar in magnitude to CloudSat over Antarctica. In the Arctic, the ERA-Interim data qualitatively
represented the interannual snowfall rates and seasonal cycle well but underestimated high snowfall rates significantly during
summer and overestimated weak snowfall rates over open water compared to CloudSat. Seasonal biases tended to be higher in
colder months when heavier snowfall occurred (Edel et al., 2020). Boisvert et al. (2020) compared different reanalysis products

120   including ERA-Interim and ERA5, and focused on snowfall in the Southern Ocean. They found similar spatial and interannual
snowfall patterns, where ERA-Interim produced the least snowfall compared to ERA5 and the other reanalysis datasets. Sea-
ice representation, atmospheric moisture content, temperature, cloud microphysics schemes, and data assimilation used in the
reanalysis were identified to all contribute to the disagreement on snowfall magnitude at lower latitudes (north of the Antarctic
continent, Boisvert et al., 2020). They also showed that the difference between subsequent reanalysis iterations is due to these

125   factors, and model resolution changes. However, it is challenging to attribute the differences further to specific factors.

  This study adds to the previous literature discussed above by connecting cloud phase and surface snowfall in ERA5 reanal-
ysis, CMIP6 models, and CloudSat-CALIPSO observations through analyses of the frequency of occurrence of sLCCs and
associated surface snowfall in these data sets. The frequency of sLCC occurrence (f_{sLCC}) represents the fraction of time (in
percent) that sLCCs are observed, while the frequency of snowfall from sLCC (f_{snow}) denotes the percentage of time that

sLCCs are snowing. This information is crucial for understanding when and where sLCCs produce snowfall and is vital for predicting and modeling precipitation patterns in high-altitude and latitudinal areas. By studying the f_{snow}, valuable insights into the occurrence of snowfall can be gained, further enhancing our understanding of its role in the water cycle, as well as the representation of the WBF process in reanalysis and ESMs.

Another novel contribution is the assessment of cloud phase biases based on a relatively new cloud phase metric that aims for

135 a like-for-like comparison with satellite retrievals to the extent possible, and the relation of these biases to associated snowfall biases in reanalysis and ESMs. The study area spans the latitudinal ranges of 45°N - 82°N and 45°S - 82°S. We select these regions because they cover the mid-latitudes and polar areas where mixed-phase clouds and surface snowfall are predominantly observed (Warren et al., 1988; Komurcu et al., 2014; Korolev et al., 2017; Matus and L'Ecuyer, 2017; Chen et al., 2020). The central research question of this study is: What are the cloud phase biases in the NH and SH mid-to-high latitudes in ERA5

140 and *historical* simulations from CMIP6 with respect to the relatively new cloud phase metrics, and how do these biases relate to snowfall biases? By addressing this research question, we aim to improve our understanding of cloud phase representation and its connection to snowfall and ultimately contribute to the advancement of climate modeling and prediction.

In the subsequent sections, we will investigate the frequency and geographic distribution of sLCCs and associated snowfall in order to distinguish their contribution to the overall snowfall patterns. Section 2 of this paper includes a description of the

145 datasets and methodologies utilized in this study. Section 3 presents the results for the f_{sLCC} and f_{snow} for the NH and SH mid-to-high latitudes, between 2007 and 2010. Section 4 is a discussion on CloudSat-CALIPSO and the use of different time sampling for the various datasets. In Section 5, the connection between cloud phase and snowfall biases is discussed and gives possible next steps for future studies.

2 Data and Methods

150 Our primary emphasis is on snow-producing sLCCs in the mid-to-high latitudes of both hemispheres. We utilize CloudSat-CALIPSO satellite observations, ERA5 reanalysis, and CMIP6 simulations to assess biases both in the spatial distribution and frequency of occurrence of sLCCs as well as their respective snowfall frequency. This section introduces the different data sets and presents the statistical methods used for the cloud phase and snowfall analysis. Table 1 lists the units and data properties for the variables used from CloudSat-CALIPSO, ERA5, and CMIP6, respectively.

2.1 CloudSat-CALIPSO Satellite Retrievals

In our investigation of the relationship between sLCCs and surface snowfall biases, we rely on satellite observations from CloudSat and CALIPSO for the comparison with ERA5 and CMIP6 models. Specifically, we use Release 5 (R05) versions of the 2B-CLDCLASS-LIDAR product (Sassen et al., 2008) for cloud phase determination, the 2C-SNOW-PROFILE product (Wood and L'Ecuyer, 2018) for the surface snowfall rate estimation, and 2m temperatures from the ECMWF-AUX data set

160 that contains ancillary ECMWF state variable data interpolated to each vertical radar bin (see Table 1).

Table 1. Overview of variable and original data field name, units, and data properties for CloudSat-CALIPSO, ERA5, and CMIP6 datasets. CMIP6 model variables represent variable short names.

Variable	Data field name	Units	Variable property
CloudSat-CALIPSO			
Cloud phase flag	CloudPhase	ice, mixed, liquid	from: 2B-CLDCLASS-LIDAR
2-metre temperature	Temperature_2m	K	from: ECMWF-AUX
Surface snowfall rate	snowfall_rate_sfc	mmh^{-1}	from: 2C-SNOW-PROFILE
ERA5			
Total column cloud liquid water	tclw	kgm^{-2}	Instantaneous
Total column rainwater	tcrw	kgm^{-2}	Instantaneous
2 metre temperature	2t	K	Instantaneous
Mean snowfall rate	msr	$\mathrm{kgm}^{-2}\mathrm{s}^{-1}$	Mean rate
CMIP6			
Mass Fraction of Cloud Liquid Water	clw	kgkg^{-1}	model level
Near-Surface Air Temperature	tas	K	single level
Snowfall Flux	prsn	$\mathrm{kgm}^{-2}\mathrm{s}^{-1}$	single level
Pressure on Model Half-Levels	phalf	Pa	model half level
Grid-Cell Area for Atmospheric Grid Variables	areacella	m^2	single level

The 2B-CLDCLASS-LIDAR product utilizes the CALIOP lidar and the CPR on CloudSat and their different sensitivities to liquid droplets and ice crystals in order to retrieve the phase of a cloudy layer. The algorithm uses a temperature-dependent radar reflectivity threshold (Zhang et al., 2010), the integrated attenuated lidar backscattering coefficient, as well as cloud base and top temperatures from atmospheric reanalysis data to discriminate between ice, mixed, or liquid water clouds (Wang

165 and Sassen, 2019). In accordance with McIlhattan et al. (2017), we focus on the phase of the bottom cloud layer within the atmospheric column and neglect the cloud phase quality flag, irrespective of the confidence level indicated. The rationale for the latter is the lidar's ability to robustly detect any liquid (liquid or mixed), and a low confidence value for the phase determination could stem from the uncertainty in the distinction between purely liquid clouds and mixed-phase clouds. This is particularly true for the frequent structure of polar mixed-phase clouds with the liquid layer at cloud top (McIlhattan et al., 2017).

170 To estimate the surface snowfall rate, we use the 2C-SNOW-PROFILE product (Wood and L'Ecuyer, 2018), which is based on an optimal estimation algorithm to retrieve profiles of parameters of the snow size distribution. The optimal estimation uses the radar reflectivity profile of the snow layer, ancillary meteorological information, and assumptions about snow microphysical and scattering properties. As the CPR cannot reliably measure near-surface reflectivities due to ground clutter, the surface snowfall rate is estimated based on the lowest clutter-free radar bin (Wood et al., 2014). The truncation height of the snow

175 profile due to ground clutter is surface dependent (2 range bins above surface over ocean (~ 500m), 4 range bins over land and sea ice (~ 1000m), Wood et al., 2014).

We focus on the years 2007 to 2010 before CloudSat switched to daytime-only operations due to a battery malfunction. Furthermore, we exclude September 2008 and December 2009 due to insufficient CALIOP data and a CloudSat battery failure (Keys, 2010). We aggregate the profile-by-profile data to a horizontal grid with a resolution of $3.75°$x$1.9°$ for each month.

180 Subsequently, we calculate the monthly f_{sLCC} and f_{snow} as described in Sect. 2.4.

The sea ice concentration (SIC) data used in this study is obtained from the Institute of Environmental Physics, University of Bremen. The data is derived using the ARTIST Sea Ice (ASI) algorithm developed by Spreen et al. (2008). The ASI retrieval method utilizes microwave radiometer data from the Advanced Microwave Scanning Radiometer for EOS instrument on the Aqua satellite and the Advanced Microwave Scanning Radiometer 2 instrument on the GCOM-W1 satellite. Both datasets

185 were reprocessed in 2018 with the same parameters. To present the 20% SIC, a seasonal average of the SIC is calculated for the years 2007 to 2010 and then gridded onto the $3.75°$x$1.9°$ grid using bilinear interpolation.

2.2 ERA5 Reanalysis

The ERA5 reanalysis data employs 4D-Var data assimilation of the ECMWF Integrated Forecast System. ERA5 incorporates an improved stratiform cloud and precipitation scheme, enhancing the representation of mixed-phase clouds compared to

190 ERA-Interim (Hersbach et al., 2020) and includes prognostic variables for both rain and snow (Forbes et al., 2011; Forbes and Tompkins, 2011; Forbes and Ahlgrimm, 2014). The meteorological values are output at a resolution of 0.25x$0.25°$.

In order to detect the presence of sLCCs in ERA5 data, specific criteria involving the T2m threshold and LWP threshold must be met (see Section 2.4). However, it is worth noting that ERA5 does not readily provide LWP values. Therefore, we calculated LWP using the total column cloud liquid water (tclw) and the total column rainwater (tcrw), expressed in kgm^{-2}

195 (Table 1). We incorporate tcrw with the 2t threshold below $0°$C, as this threshold is used to exclude any rainwater below the melting layer. By using tclw and tcrw and applying the temperature threshold, we can analyze the role of supercooled liquid water within clouds and the contribution of liquid water to the snowfall precipitation process in ERA5.

To calculate the f_{snow}, we rely on the mean snowfall rate variable (msr, Table 1). The mean snowfall rate, expressed in units of $kgm^{-2}s^{-1}$, provides a combined measurement of both large-scale and convective snowfall. It is calculated as an average over

200 24 hours. Here we use the ERA5 CDS tool to average all of the output variables into daily mean values based on hourly data (Cucchi et al., 2021; C3S, 2020-11-12). It is important to note that 2t, tclw, and tcrw (Table 1) are reported as instantaneous values every hour, meaning that when they are averaged to obtain daily mean values, they may not accurately represent the actual daily mean values. Nevertheless, a non-zero model daily mean LWP means there was an LCC in the grid box at some point during the day. In contrast, the mean snowfall rate is reported as a temporal average and accurately represents the daily

205 mean snowfall rate.

2.3 CMIP6 Models

Our inter-model comparison relies on data from CMIP6, which involves simulations from various modeling centers. Specifically, we focus on the *historical* simulations (1850-near present, Eyring et al., 2016), selecting ten models with daily mean outputs from different ensemble members as outlined in Table A1. In most of the figures shown in this study, we present the
210   CMIP6 multi-model mean.

In our analysis, we consider the following variables (Table 1): mass mixing ratio of cloud liquid water (clw), encompassing liquid water in both large-scale and convective clouds provided at each model level in units of $\mathrm{kgkg^{-1}}$. Precipitating hydrometeors within the clw variable are included only if they affect the model's radiative transfer calculations. Near-surface air temperature (tas), reflecting the temperature at a height of 2 meters above the surface, measured in Kelvin; and snowfall flux
215   (prsn), representing precipitation in all forms of frozen water, expressed in $\mathrm{kgm^{-2}s^{-1}}$.

As none of the models listed in Table A1 directly provide LWP as a daily output variable, we derive LWP based on clw. To calculate the LWP, we interpolate the CMIP6 hybrid-sigma pressure to isobaric pressure (Sec.A). The UKESM1-0-LL and HadGEM3-GC31-LL models provide values on orographic vertical coordinates. Consequently, for these models, we use the CMIP6 variable phalf (Table 1) instead of calculating isobaric pressure levels. Subsequently, we utilize the hydrostatic
220   equation to calculate the liquid water content for each vertical grid box. The liquid water content is then summed up over the vertical to obtain the LWP for each horizontal grid box (see Section A).

CMIP6 data is gathered from 2006 to 2009 as these years represent the closest available overlapping time range for all CMIP6 models (some models ended the simulations by December 2009, marked with an asterisk in Table A1). The slight mismatch in the time range is of limited relevance, as CMIP6 model simulations are not designed to reproduce the exact temporal evolution of past weather but instead generate their own internal variability (e.g., ENSO cycles), so they should only be viewed as generally representative for the time period in question.

2.4 Calculation of $\mathrm{f_{sLCC}}$ and $\mathrm{f_{snow}}$

The instrument sensitivities of the CPR and CALIOP, as well as their different temporal and spatial sampling in contrast to the gridded ERA5 and CMIP6 data, require different metrics that ensure a like-for-like comparison to the extent possible. In
230   the following, we describe the calculation of these metrics ($\mathrm{f_{sLCC}}$ and $\mathrm{f_{snow}}$) and call attention to differences between the satellite observations and ERA5 or CMIP6. For ERA5 and for CMIP6 models, we remap all models to the coarsest resolution of $3.75° \times 1.9°$, which corresponds to the grid of IPSL-CM5A2-INCA (Table A1) with a nominal resolution of approximately $500\mathrm{km}$. We use area-weighted averages for both the NH and SH to calculate spatial means.

2.4.1 Frequency of sLCC

235   We defined the occurrence of a sLCC in a cloudy CloudSat-CALIPSO profile when the lidar detected any liquid in the lowermost cloud layer (phase flag *liquid* or *mixed*), and the surface temperature was below freezing ($\mathrm{Temperature\_2m} \leq 0°C$). The temperature threshold was applied to ensure that the clouds were supercooled. In ERA5 and CMIP6, we applied the same

Table 2. Calculation of f_{sLCC} and f_{snow} and overview of applied thresholds. The first rows correspond to CMIP6/ERA5 metrics, while rows denoted with 'CC' describe CloudSat-CALIPSO metrics.

Variable Name	Description	Thresholds and equations
N_all	Number of all days	
	CC: Number of all observations	
N_sLCC	Number of days with sLCCs	$T2m \leq 0°C$, LWP$\geq$5gm^{-2}
	CC: Number of observations with sLCCs	$T2m \leq 0°C$, phase flag liquid/mixed
N_sLCC_sf	Number of days with snowing sLCCs	sf ≥ 0.01kgm^{-2}h^{-1}
	CC: Number of observations with snowing sLCCs	sf ≥ 0.01kgm^{-2}h^{-1}
f_{sLCC} (%)	Frequency of sLCCs	N_sLCC / N_all
f_{snow} (%)	Frequency of snowing sLCCs	N_sLCC_sf / N_sLCC

temperature threshold and defined an sLCC when the LWP is above 5gm^{-2}. This is in accordance with McIlhattan et al. (2017) and based on their sensitivity estimate when comparing CloudSat with ground-based microwave radiometer observations at

240   Summit, Greenland. This definition of sLCCs is likely a very conservative estimate of the actual frequency of clouds containing supercooled liquid in the atmosphere because we require temperatures below freezing at the surface, while, in reality, there could still be supercooled liquid even if the surface is above freezing. However, as we are investigating the frequency of snowing sLCCs in the second part of this study, we want to ensure that any precipitation from the sLCCs is primarily in the form of snow.

245   In ERA5 and CMIP6, we calculate f_{sLCC} as the number of days with sLCCs present (N_sLCC) divided by the total number of days (N_all) over a specific time period (see Table 2). However, we cannot utilize daily statistics on a global scale from CloudSat-CALIPSO due to their transect-based sampling in combination with a revisit time of 16 days and, consequently, insufficient horizontal coverage (e.g., Kotarba, 2022; von Lerber et al., 2022). Thus, after aggregating the CloudSat-CALIPSO profiles to the same grid as ERA5 and CMIP6, we calculate f_{sLCC} from satellite by dividing the number of profiles in that

250   month with an sLCC by the total number of profiles (see Table 2).

2.4.2   Frequency of Snowfall in sLCCs

For the occurrence of snowfall from sLCCs, we define a snowfall threshold of 0.01kgm^{-2}h^{-1}. Again, this is based on McIlhattan et al. (2017) and aims to mitigate biases due to instrument sensitivities. The f_{snow} in ERA5 and CMIP6 is then calculated as the number of days with snowfall (N_sLCC_sf) divided by the total number of days with sLCCs present (N_sLCC, see

255   Table 2). The ERA5 and CMIP6 snowfall rates and $T2m$ are given as daily mean values. It is important to note that as f_{sLCC} is calculated using daily mean values, the simulated precipitation can, in principle, occur as rain (or supercooled rain) depending on the temperature at the time of the precipitation. However, as no additional information is available, we here assume that
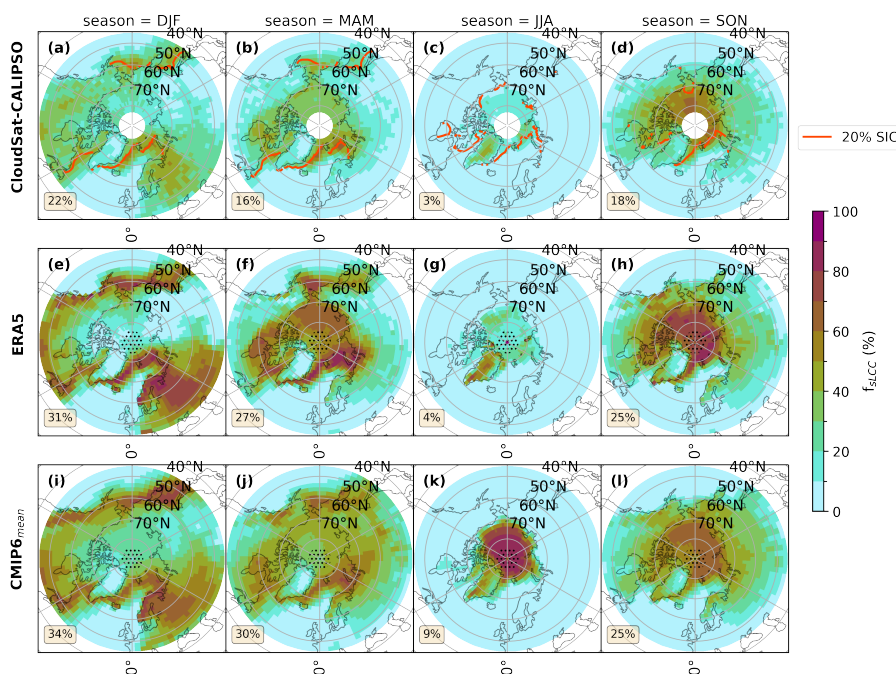
Figure 1. The NH mid-to-high latitude seasonal averages of f_{sLCC}. The first row (a-d) for CloudSat-CALIPSO, the second row (e-h) displays ERA5 data, and the third row (i-l) shows the CMIP6 model mean. Each map includes an area-weighted average for the study area (lower left corner). These averages are calculated for areas where CloudSat-CALIPSO have valid observations (between $45°N - 82°N$) and exclude the dotted area (in e-l). The red line (in a-d) shows the average sea ice edge of 20% sea ice concentration (SIC) between 2007 and 2010, for the given season.

all precipitation from sLCCs is in the form of snow. To ensure comparability among the three datasets (CloudSat-CALIPSO, ERA5, and CMIP6), we perform a unit transformation, as outlined in Section B.

260   To account for the differences in sampling in space and time, we calculate f_{snow} from CloudSat-CALIPSO as the number of observations with snowing sLCCs divided by the number of observations with sLCCs (Table 2).

3   Results

The following subsections examine and intercompare f_{sLCC} and f_{snow}, respectively, from the three data sets examined (CloudSat-CALIPSO, ERA5 and CMIP6 models).

265 ### 3.1   Frequency of sLCCs

Fig. 1 a-d presents the seasonal variability of f_{sLCC} observed by CloudSat-CALIPSO in the mid-to-high latitudes of the NH. Evident from the figure is a clear seasonal progression in the spatial distribution of f_{sLCC}. In summer (JJA), f_{sLCC} reaches its

minimum spatial average, with non-negligible values primarily within the Arctic basin. In NH autumn (SON), f_{sLCC} values increase significantly in the Arctic basin but also spread to land areas pole-ward of about $60°$N. In boreal winter (DJF),

270 maximum values shift away from the Arctic basin and are instead found over the ocean close to the average seasonal sea ice edge (Fig. 1 a, red line).

The Greenland ice sheet (GRIS) is a region of particular interest for this study, as sLCCs have been proposed to accelerate GRIS surface melt (Bennartz et al., 2013; Hofer et al., 2019), while snowfall represents the primary ice sheet growth mechanism. The GRIS, which is characterized by its high elevation and snow-covered surface, experiences numerous sLCCs during

275 boreal summer and autumn due to sufficient moisture and temperatures below $0°$C in the CloudSat-CALIPSO observations (Fig. 1 c, d). However, during boreal winter and spring (MAM), the f_{sLCC} is low ($< 15\%$) as the region becomes too dry and cold (Shupe et al., 2013) to support the formation of sLCCs. The seasonal cycle of f_{sLCC} as observed by CloudSat-CALIPSO is largely what would be expected from the combined seasonal influence of atmospheric circulation, moisture availability, and temperature conditions in the mid-to-high-latitudes in the NH.

280 Comparing the CloudSat-CALIPSO observations with ERA5 and the CMIP6 model mean, we generally observe that ERA5 and the CMIP6 models show a similar seasonal progression of f_{sLCC} to that seen in the satellite observations. However, both ERA5 and the CMIP6 mean overestimate f_{sLCC} to various extents during all seasons. The most significant discrepancy is observed during boreal spring, with area-weighted averaged differences between CloudSat-CALIPSO and ERA5, and the CMIP6 model mean of -11% and -14%, respectively (Fig. C1 f, j). Nevertheless, the spatial extent of areas with f_{sLCC}

285 values larger than 0% in CloudSat-CALIPSO is replicated well in ERA5 and the CMIP6 model mean (Fig. 1). Although ERA5 and the CMIP6 models have remarkably similar spatial patterns of f_{sLCC}s, the CMIP6 model mean generally exhibits slightly larger area-weighted biases in the NH ($6\% - 14\%$, Fig. C1 i-l) than ERA5 ($1\% - 11\%$, Fig. C1 e-h) when compared to CloudSat-CALIPSO.

The fact that these discrepancies are about equally present in both ERA5 and CMIP6 models provides valuable insights

290 into their potential causes. They are most likely linked to the microphysical parametrizations of cloud processes that govern cloud phase in ERA5 and CMIP6 models. We can safely assume the temperature to be similar between the ECMWF-AUX product used in CloudSat-CALIPSO and ERA5 daily mean, while atmospheric circulation and overall cloud cover should be well constrained by the observations used in the ERA5 reanalysis. However, the cloud phase is not as evident in the identified biases. This finding will be discussed in greater depth in Section 5.1.

295 Unlike the NH mid-to-high latitudes, the SH does not experience significant seasonal variations in f_{sLCC}, according to the CloudSat-CALIPSO observations (Fig. 2 a-d). The f_{sLCC} remains relatively constant across all seasons and is the highest in a band bounded by the Antarctic continent in the South and approximately the $60°$ parallel in the North, with values between $17\% - 24\%$. However, the area-weighted averages of f_{sLCC} in the SH are generally higher than in the NH. The relatively constant f_{sLCC} indicates that a more persistent cloud regime exists in the SH, with extensive sLCC cover present all year

300 round. This is consistent with previous literature reporting that the Southern Ocean is the region of the world with the most extensive mixed-phase cloud cover (Matus and L'Ecuyer, 2017).
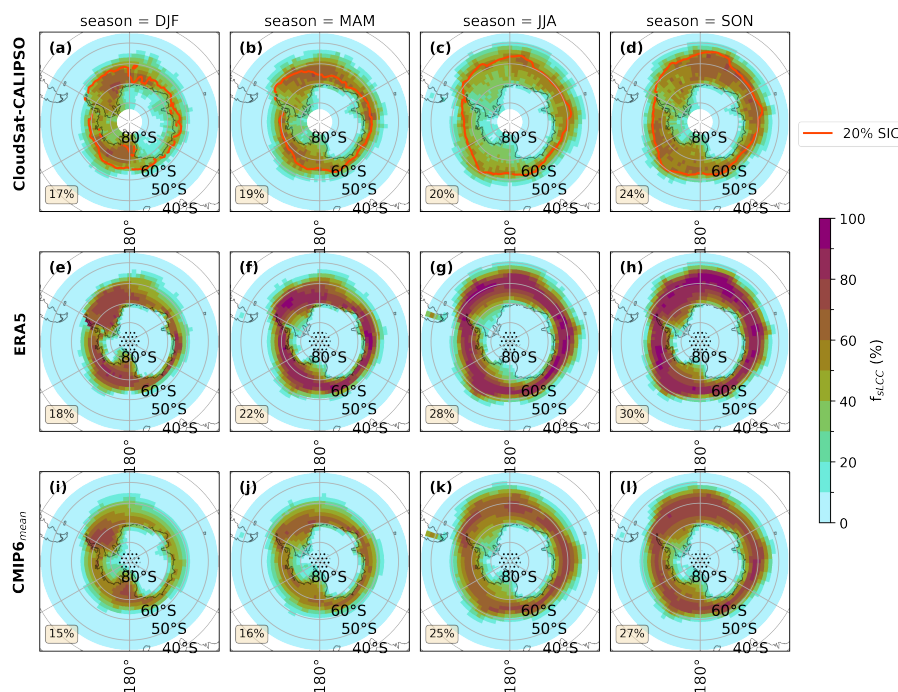
Figure 2. The SH mid-to-high latitude seasonal averages of f_{sLCC}. The first row (a-d) for CloudSat-CALIPSO, the second row (e-h) displays ERA5 data, and the third row (i-l) shows the CMIP6 model mean. Each map includes an area-weighted average for the study area (lower left corner). These averages are calculated for areas where CloudSat-CALIPSO have valid observations (between $45°S - 82°S$) and exclude the dotted area (in e-l). The red line (in a-d) shows the average sea ice edge of 20% sea ice concentration (SIC) between 2007 and 2010, for the given season.

Like the GRIS, the Antarctic ice sheet has a low f_{sLCC} with the lowest frequency in austral winter (JJA, $\leq 15\%$). With its high elevations, the East Antarctic ice sheet exhibits a lower f_{sLCC} than the flatter West Antarctic Ice Sheet during austral summer (DJF), autumn (MAM), and spring (SON). Just like the NH, the SH shows a reduced area of f_{sLCC} in austral summer (Fig. 2 c), but with a larger extent towards lower latitudes (NH: $> 70°N$, SH: $> 60°S$). In all seasons, f_{sLCC} are observed primarily southward of the Antarctic Circumpolar Current, which may be due to the presence of warm water that results in surface temperatures above the sLCC threshold (Fig. 2 a-d).

In both ERA5 and the CMIP6 model mean, there is a prominent gradient of sLCCs between the Southern Ocean and the Antarctic ice sheet with f_{sLCC} of up to 100% over the Southern Ocean and $< 15\%$ over the Antarctic ice sheet. For the SH spatial mean, ERA5 and CMIP6 model mean moderately overestimate f_{sLCC} ($1\% - 8\%$), with the CMIP6 model mean, in general, performing slightly better than ERA5 in comparison to CloudSat-CALIPSO (Fig. C2).

The biases in ERA5 and the CMIP6 models regarding f_{sLCC}, relative to CloudSat-CALIPSO, are further demonstrated through the area-weighted averages for each month in both hemispheres (Fig. 3). For the area-weighted averages, we consider only the locations where CloudSat-CALIPSO provided valid data (values between $|45° - 82°|$). CMIP6 models generate a
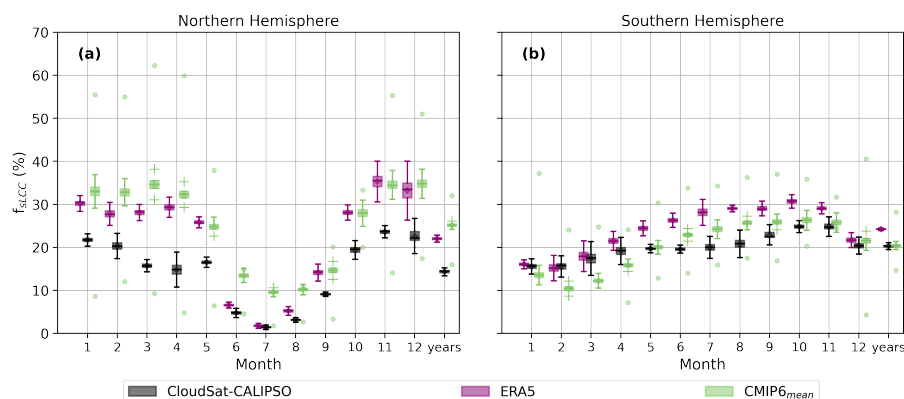
Figure 3. The annual cycle of monthly f_{sLCC} for (a) NH ($45°$N-$82°$N), and (b) SH ($45°$S and $82°$S). Shown are area-weighted averages for CloudSat-CALIPSO (black), ERA5 (pink), and the CMIP6 model mean (green). Each box represents the interquartile range (IQR) from the 25th to the 75th percentile. The whiskers extend to the minimum and maximum values, defined as the 25th percentile minus 1.5 times the IQR and the 75th percentile plus 1.5 times the IQR, respectively. Any points falling outside these whiskers are considered outliers and are marked with crosses. The green dots represent the minimum and maximum CMIP6 model values over all years.

315   large spread of f_{sLCC}, with both CloudSat-CALIPSO and ERA5 falling within the range of the model maximum and minimum values (green dots in Fig. 3). Again it is evident that ERA5 and the CMIP6 model mean have higher f_{sLCC} than CloudSat-CALIPSO in the NH (Fig. 3 a). The SH area-weighted averages show a better agreement between CloudSat-CALIPSO, ERA5, and CMIP6 model mean than in the NH (Fig. 3 b). The CMIP6 model mean underestimates f_{sLCC} in comparison to CloudSat-CALIPSO during austral summer and autumn, but overestimates during winter and spring, while ERA5 overestimates f_{sLCC}

320   to various degrees all year round in the SH.

     Finally, to assess the model performance relative to CloudSat-CALIPSO for ERA5 and the individual CMIP6 models for f_{sLCC}, we analyze the absolute difference in seasonal and spatial averages for each of the 11 models (Fig. 4) for the NH and SH mid-to-high latitudes. The most significant discrepancy is seen in boreal winter and spring for AWI-ESM-1-1-LR, MPI-ESM1-2-LR, and IPSL-CM6A-LR with an absolute difference $> 15\%$ (Fig. 4 a). In the NH, MPI-ESM1-2-LR is generally the model with the larger overestimation ($> 15\%$), despite in boreal summer with an absolute difference of $< 10\%$. IPSL-CM5A2-INCA

325   has a low absolute difference, $< 5\%$ in boreal summer, autumn, and winter. As previously highlighted, the absolute difference values for f_{sLCC} are lower in the SH (Fig. 4 b), and none of the models stand out in terms of overall performance in either direction.

3.2   Frequency of Snowfall from sLCC

330   To assess the ability of ERA5 reanalysis and the CMIP6 models to represent snowfall processes, we compare the f_{snow} between them and the CloudSat-CALIPSO observations. Based on CloudSat-CALIPSO observations, NH sLCCs frequently produce snowfall, as can be seen by the non-zero values of f_{snow} in Fig. 5 a-d. However, during boreal summer, the majority of sLCC
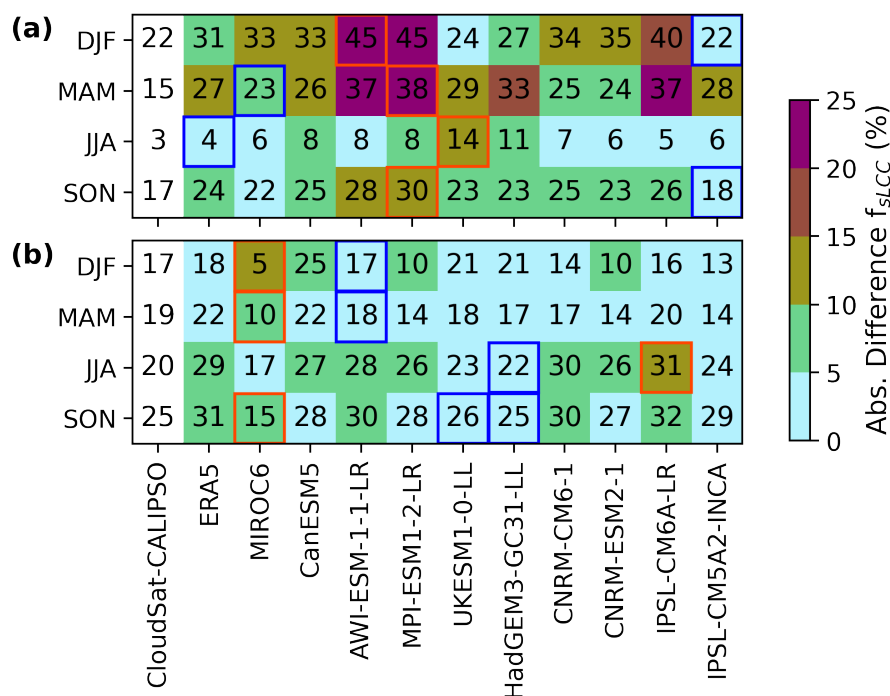
Figure 4. Seasonal area-weighted averages (between $|45° − 82°|$) of f_{sLCC} for CloudSat-CALIPSO, ERA5, CMIP6 models (numbers). The heatmap colors correspond to the absolute differences of area-weighted averages of f_{sLCC} between CloudSat-CALIPSO and ERA5 and CMIP6 models. (a) for the mid-to-high latitude NH, and (b) for the mid-to-high latitude SH. Per season, the smallest (largest) absolute seasonal and spatial differences are outlined with blue (red) lines.

rarely produce snowfall, as shown by the relative increase in the areal extent of zero f_{snow} values (Fig. 5 c). Notably, during boreal winter, spring, and autumn, the seasonal average f_{snow} is highest over open ocean regions, such as the Greenland, Norwegian, and Barents Sea ($30% − 65%$), the Labrador Sea ($40% − 80%$), and the Bering Sea ($40% − 100%$, Fig. 5 a, b, d). This is likely due to plentiful available moisture for snowfall to occur and possibly linked to Cold Air Outbreaks (CAOs) (Young et al., 2017). CAOs arise when cold, dry air flows over warmer, moist sea surfaces. CAOs occur frequently in the North Atlantic in boreal winter and spring, and the clouds associated with them are predominantly sLCCs (Fletcher et al., 2016; Papritz and Sodemann, 2018; Geerts et al., 2022; Mateling et al., 2023). While the signature of CAOs is also visible in the f_{snow} patterns, besides in boreal summer, land areas have lower values as these areas warm in response to increased insolation.

In contrast to the CloudSat-CALIPSO observations, both ERA5 and the CMIP6 model mean have much higher f_{snow} values ($> 60%$), which are evenly distributed over the NH mid-to-high latitudes, without a significant seasonal variability. In regions where all three datasets have sLCCs, ERA5 and the CMIP6 model mean overestimate the f_{snow} by $\sim 50%$ (Fig. C3). This indicates that ERA5 and the CMIP6 models produce snowfall much more frequently from sLCC than observed. It is important
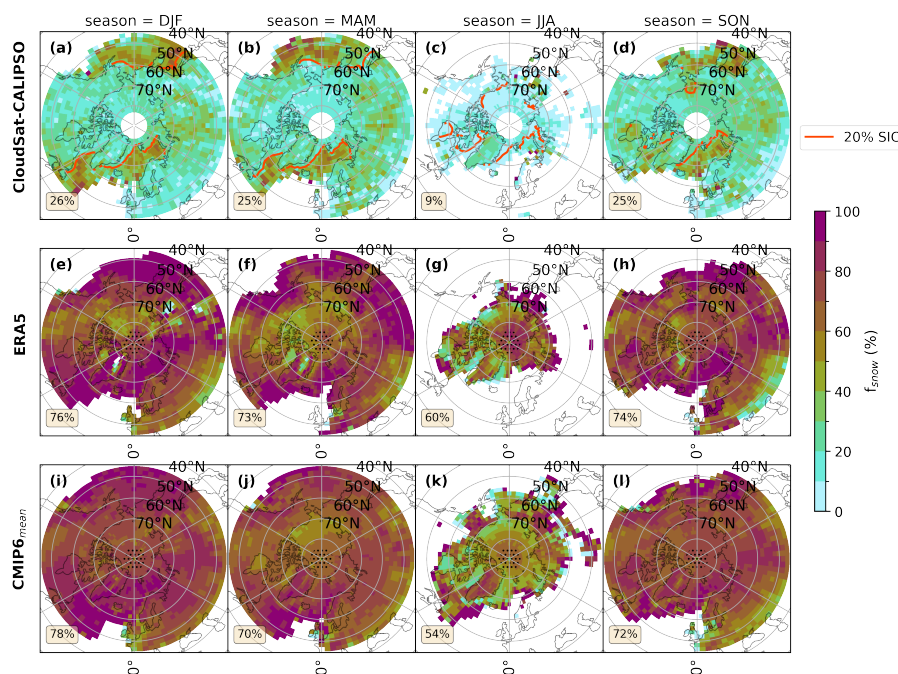
Figure 5. The figure presents the seasonal averages of f_{snow} in the NH mid-to-high latitudes. The layout and area-weighted averages are calculated the same as those shown in Figure 1.

345   to note that since f_{snow} accounts for the number of sLCCs, ERA5 and the CMIP6 models are too efficient in producing snowfall regardless of the number of sLCCs that are simulated/assessed.

    Regarding the SH mid-to-high latitudes, the CloudSat-CALIPSO observations show that there is no significant seasonal variation in f_{snow}, with spatially averaged values of $\sim 20\%$ for all seasons (Fig. 6 a-d). However, when comparing the results from ERA5 and the CMIP6 model mean with observations from CloudSat-CALIPSO, we find that similar to the NH, the simulated

350   f_{snow} values are much higher than those observed (Fig. 6). When considering only regions where CloudSat-CALIPSO observes f_{snow} ($45°S - 82°S$), the area-weighted seasonal average of f_{snow} is approximately $60\% - 70\%$ higher in ERA5 and the CMIP6 model mean (Fig. C4). The high simulated values of f_{snow} in both the NH and SH indicate that ERA5 and CMIP6 models produce snowfall far too frequently from sLCCs compared to the satellite observations. In fact, when sLCCs are present, snow is produced practically all of the time (between 70% and 90%). This bears resemblance to a well-established bias in ESMs,

355   namely the persistent "perpetual drizzle" problem for warm liquid clouds (Mülmenstädt et al., 2020; Lavers et al., 2021).

    To investigate the annual cycle of f_{snow} and the interannual variation between 2007 and 2010, we present the area-averaged data based on grid boxes where CloudSat-CALIPSO is capable of making observations ($|45° - 82°|$, Fig. 7). CloudSat-CALIPSO displays a relatively clear seasonal cycle in f_{snow} in the NH, but not in the SH. The difference in the f_{snow} between boreal summer months and the rest of the year in the NH is 15%, while the SH value is constant around 20% throughout

360   the year. In contrast, ERA5 and the CMIP6 model mean display a more significant seasonal cycle, with a difference of 25%
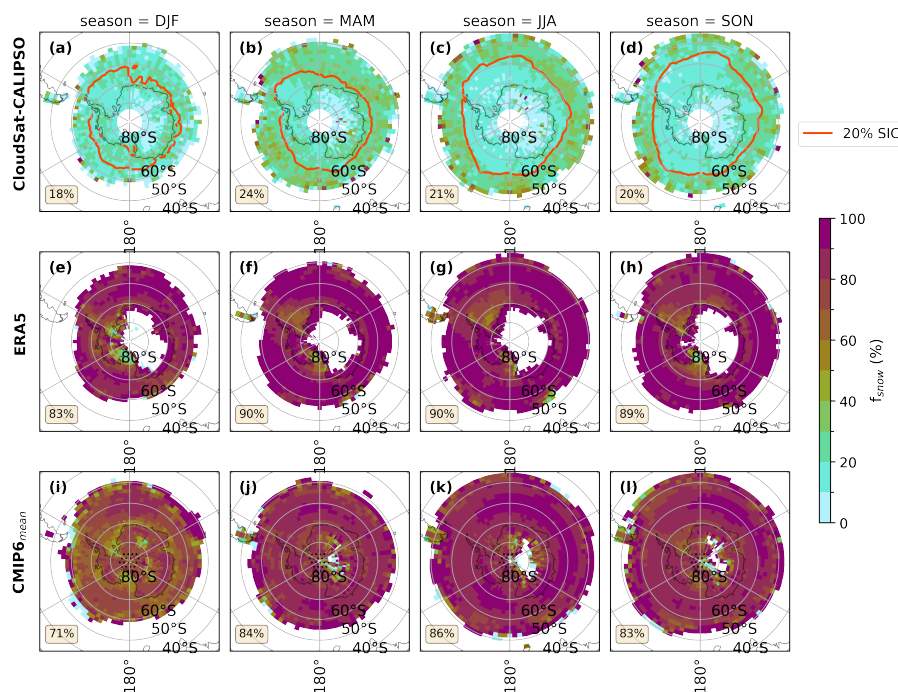
Figure 6. The figure presents the seasonal averages of the f_{snow} in the SH study region. The layout and area-weighted averages are calculated the same as those shown in Figure 1.
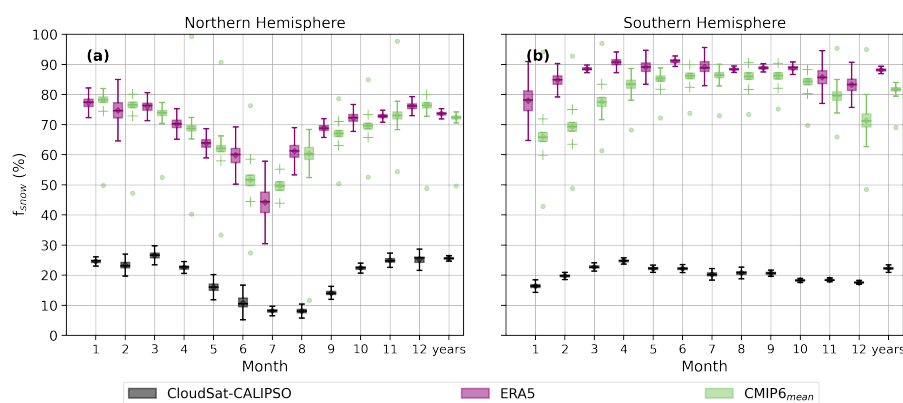
Figure 7. Annual cycle of f_{snow} for (a) the NH, defined here as the region between $45°N$ and $82°N$ and (b) SH, defined here as the region between $45°S$ and $82°S$. Colors and boxplots are identical to Figure 3.

between boreal summer and winter months (Fig. 7 a). Also, in the SH, there is more of a seasonal cycle evident for ERA5 and the CMIP6 model mean. Also worth noting is that ERA5 shows more pronounced interannual variability in both hemispheres
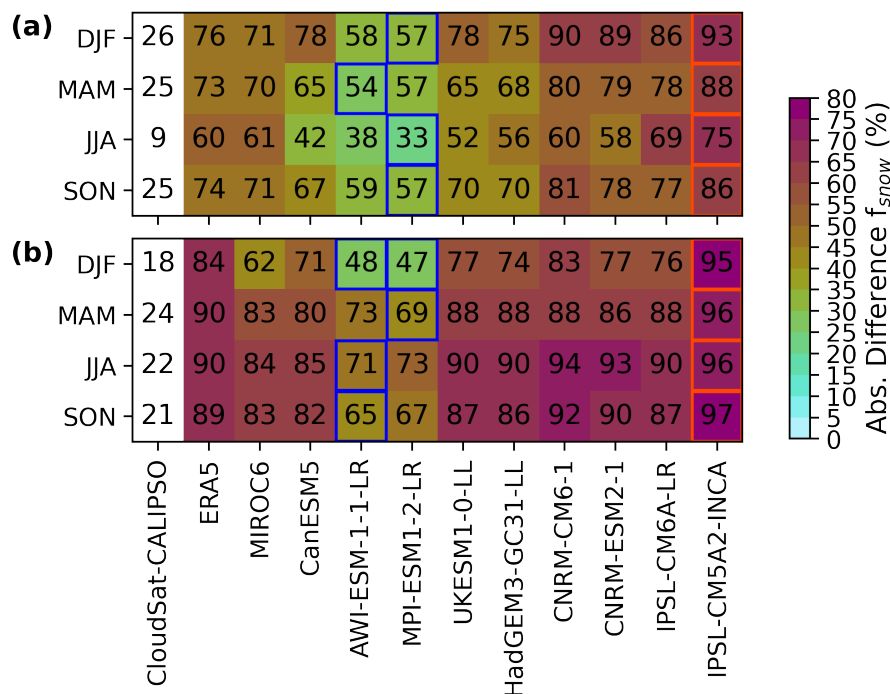
Figure 8. Seasonal area-weighted averages (between $|45° − 82°|$) of f_{snow} for CloudSat-CALIPSO, ERA5, CMIP6 models (numbers). The heatmap colors correspond to the absolute differences of area-weighted averages of f_{snow} between CloudSat-CALIPSO and ERA5 and CMIP6 models. (a) for the mid-to-high latitude NH, and (b) for the mid-to-high latitude SH. Per season, the smallest (largest) absolute seasonal and spatial differences are outlined with blue (red) lines.

of f_{snow} for a given month, meaning that the year-to-year fluctuations are larger than for CloudSat-CALIPSO and the CMIP6 model mean.

365   The comparison of absolute differences for f_{snow} in Fig. 8 indicates how well the individual ESMs represent the frequency of occurrence for snow, and if the same models that perform well for f_{sLCC} (Fig. 4) do so for surface snowfall as well. Among the models, AWI-ESM-1-1-LR and MPI-ESM1-2-LR come closest to matching CloudSat-CALIPSO observations, but their f_{snow} are still much too high (NH: $\sim 30\%$, SH: $\sim 45\%$, Fig. 8). At the same time, IPSL-CM5A2-INCA deviates the most for f_{snow} in the NH and SH, having an absolute difference of $\sim 65\%$ and $\sim 75\%$, respectively. Interestingly, it appears that some
370   models that perform well for f_{sLCC} perform poorly for f_{snow}. This could be an indication that models that are able to simulate the right frequency of occurrence of sLCCs can do so because they are converting cloud condensate to snow too readily. In other words, models may be getting the right answer for the wrong reason.

4 Sensitivity tests

In the previous section, we examined the frequency of occurrence of sLCCs (f_{sLCC}) and the frequency of occurrence of surface

375 snowfall (f_{snow}) from sLCCs in CloudSat-CALIPSO, ERA5, and CMIP6 data, and found that the reanalysis and ESMs have too many sLCCs and too frequent surface snowfall in comparison to CloudSat-CALIPSO. The identified biases are large, and the implications for our ability to predict how sLCCs and snowfall might change with future warming are potentially significant. It is therefore important to ensure that these findings are robust, and not overly reliant on subjective decisions or limitations in the design of the comparison. In the following subsections, we investigate whether the identified discrepancies between the

380 observations on one hand and ERA5 and the CMIP6 models on the other can be explained by sampling biases or instrument sensitivity.

It is important to acknowledge that CloudSat-CALIPSO data come with inherent uncertainties, including those associated with snowfall retrievals (Stephens and Kummerow, 2007; Hiley et al., 2011; Schirmacher et al., 2023). CloudSat surface snowfall is subject to sampling biases and ground clutter issues and also relies on ECMWF temperature data to differentiate

385 between snowfall and rainfall (Boisvert et al., 2020). Milani et al. (2018) found that applying adjustments and a temperature threshold to the CloudSat snowfall retrieval led to a decrease in the estimated occurrence of snowfall events, primarily in the ocean regions surrounding Antarctica. Although these adjustments did not have the same effects everywhere, this highlights the sensitivity of the CloudSat retrievals to the assumptions made within them.

In addition to the uncertainties in the assumptions used in retrievals, comparing satellite observations with ESMs is challeng-

390 ing due to several factors linked to the sampling bias of the CloudSat-CALIPSO mission. Numerous considerations come into play when deriving climate statistics from satellite transects (Kotarba, 2022). These encompass the narrow swath coverage, infrequent revisits, and latitude-dependent ground track density (Kotarba, 2022; von Lerber et al., 2022). Varying the domain size and time scales of CloudSat observations showed that data on smaller scales or shorter time periods can introduce significant uncertainties associated with cloud, aerosol, or atmospheric properties (Henderson et al., 2013). However, instantaneous errors

395 (using satellite data on smaller scales or shorter periods) tend to cancel out over longer time periods (Henderson et al., 2013; von Lerber et al., 2022). Another limitation of space-based remote sensing observations is the uncertainty associated with the retrieval method employed to derive the snowfall rate from radar reflectivity measurements (Kulie and Bennartz, 2009; Milani et al., 2018). However, in our study, we examine frequencies of occurrence and only use the surface snowfall amount to classify if an sLCC is snowing ($sf \geq 0.01 \mathrm{kgm}^{-2}\mathrm{h}^{-1}$) or not. Such a binary variable should be less sensitive to the exact snowfall rate

400 retrieval. Edel et al. (2020) presented a CloudSat snowfall climatology, the frequency of snow, and snowfall rates over the Arctic. They found that the distribution of snowfall rate does not always match the distribution of snowfall frequency in CloudSat. Nevertheless, future modeling studies should ideally use the Cloud Feedback Model Intercomparison Project Observation Simulator Package (COSP, Bodas-Salcedo et al., 2011) to make satellite observations and model datasets more comparable. At present, COSP output is not available for a sufficient number of models and at a high enough temporal resolution to be useful

405 for the present study.
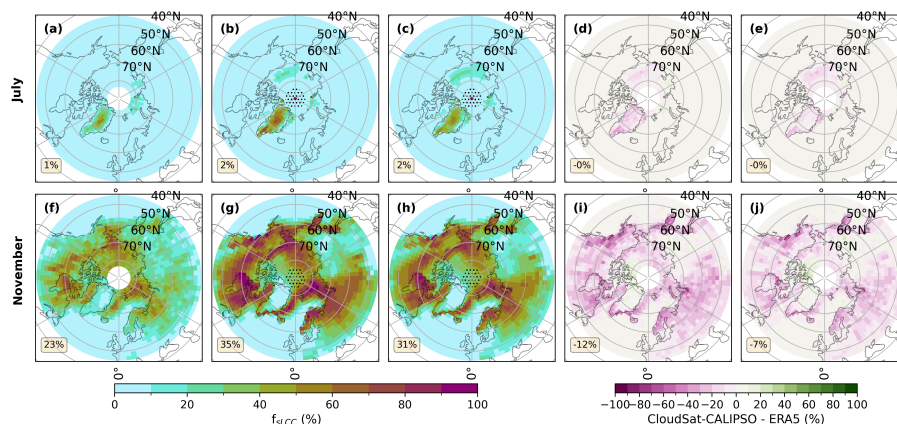
Figure 9. NH mid-to-high latitude monthly averages of f_{sLCC} for July (a-e) and November (f-j) 2007 to 2010. The columns show the CloudSat-CALIPSO monthly means (a, f), ERA5 monthly means based on daily average values (b, g), and ERA5 monthly means based on hourly values (c, h). The fourth and fifth columns are the difference plots between CloudSat-CALIPSO and the ERA5 daily averages (d, i) and ERA5 hourly values (e, j), respectively. In the last three columns, green (pink) values indicate underestimation (overestimation) with respect to the reference used. Area-weighted averages for the study area ($45°N - 82°N$) are located in the lower-left corner of each map and exclude the dotted area (in b, c, g, h).

Nevertheless, these satellite observations serve as valuable tools for identifying potential biases in reanalysis and ESMs, as demonstrated by previous studies (e.g., McIlhattan et al., 2017; Milani et al., 2018; Daloz et al., 2020; Heymsfield et al., 2020; Boisvert et al., 2020). To test the robustness of the overall findings of this study to our comparison approach, we next want to show how different temporal resolutions of ERA5, as well as different LWP thresholds applied to the CMIP6 data, impact the
410 results.

4.1 Sensitivity to ERA5 temporal resolution

In the comparison by McIlhattan et al. (2017), the analysis was performed on a 6-hourly instantaneous model output to define the occurrence of LCCs in CESM-LE. As we compare ERA5 and CMIP6 models to CloudSat-CALIPSO, we only have daily means of LWP available. Thus, instead of four instantaneous values per day for a given model grid box, we use only one
415 daily mean value of LWP. This way, we are comparing 30 daily values from ERA5 and CMIP6 models with thousands of CloudSat-CALIPSO profiles within each grid box to calculate f_{sLCC}. Due to the 16-day repeat cycle of CloudSat-CALIPSO, we cannot perform the satellite analysis on a daily temporal resolution at the given spatial resolution of the models. While CMIP6 output is not available at a higher temporal resolution, for ERA5, we can actually test the sensitivity using an even higher time resolution than McIlhattan et al. (2017). We take the hourly outputs from ERA5 from July and November 2007
420 to 2010 and create monthly mean values. July and November are chosen as these are the months with the lowest and highest f_{sLCC} in CloudSat-CALIPSO (Fig. 3 a). We find that the f_{sLCC} values emerging from ERA5 data are not very sensitive to the output frequency, as shown in Figure 9 (d-e, i-j). The area-weighted difference between CloudSat-CALIPSO and ERA5 hourly
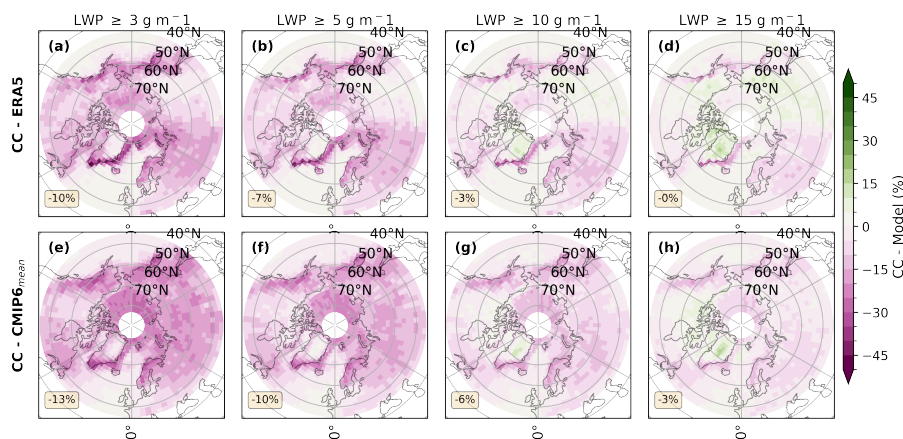
Figure 10. Annual average difference plots (CloudSat-CALIPSO (CC) minus model) for f_{sLCC} in the NH mid-to-high latitudes. The first row represents ERA5 data (a-d), and the second row shows the CMIP6 model mean (e-h) difference. LWP thresholds applied of $3gm^{-2}$ (a, e), $5gm^{-2}$ (b, f), $10gm^{-2}$ (c, g), and $15gm^{-2}$ (d, h). The analysis in this study focuses on the LWP threshold of $5gm^{-2}$. The maps in each row are accompanied by area-weighted averages for the study area, located in the lower-left corner of each map. The averages are calculated for areas where CloudSat-CALIPSO observations have valid f_{sLCC} values.

values is negligible in July (1%) and $\sim 15\%$ in the inner Arctic and reduces from 12% overestimation to 7% in November depending on the region. However, the conclusion that ERA5 overestimates the f_{sLCC} does not change by changing to a higher

425 time resolution (Fig. 9). This would most likely also hold for the CMIP6 models, although this cannot be confirmed.

4.2 Sensitivity to LWP threshold for CMIP6 models

McIlhattan et al. (2017) conducted a similar analysis as in this study by examining the frequency of Arctic LCCs and f_{snow}. They experimented with different LWP thresholds. Specifically, they used the $5gm^{-2}$ and $0.01gm^{-2}$ thresholds and based their LWP threshold of $5gm^{-2}$ on the approximate retrieval uncertainty of LWP from ground-based microwave radiometer

430 observations. We performed sensitivity tests in which we varied the threshold between 3, 5, 10, and $15gm^{-2}$ (Fig. 10). While some of these values are unreasonably high, it is nevertheless useful to test how adjusting the LWP threshold value affects the identified bias between the observations and simulations. As expected, Figures 10 and D1 indicate that as the LWP threshold increases, the overestimation of f_{sLCC} decreases both in the NH and SH. However, unless we increase the LWP threshold in ERA5 and in the CMIP6 models to an unrealistically high value, the general findings and conclusions hold - ERA5 and the

435 CMIP6 model mean still overestimate the occurrence of sLCCs in the study area in comparison to CloudSat-CALIPSO.

5 Discussion and Conclusion

We find that mid-to-high latitude sLCCs and snowfall are produced more frequently in ERA5 and CMIP6 than in CloudSat-CALIPSO. While previous studies have focused on the underestimation of supercooled liquid fraction (SLF) in mixed-phase

clouds (Komurcu et al., 2014; Cesana et al., 2015; Tan and Storelvmo, 2016; Kay et al., 2016; Bruno et al., 2021; Shaw et al.,
440 2022), this research focuses on the frequency of occurrence of sLCCs. This difference in the cloud phase metric can lead to
seemingly contradicting conclusions. We illustrate why our results do not necessarily contradict previous findings with the
following example: If an ESM consistently predicts a low percentage of liquid in clouds, while satellite observations suggest
that liquid occurs only 50% of the time but with a high liquid percentage when it does occur, it can create a discrepancy
between the metric used here and other cloud phase metrics like SLF. Even though the model would then have an sLCC
445 frequency of occurrence of 100%, the amount of supercooled liquid could still very well be underestimated. When combined
with previous studies finding that ESMs generally underestimate SLF, our findings suggest that models too frequently simulate
genuinely mixed-phase clouds with both phases present at the same time and point, while observations more frequently reveal
conditionally mixed conditions, in which ice and liquid are separated in time and/or space (Korolev and Milbrandt, 2022).

5.1 Links between biases in f_{sLCC} and f_{snow}

450 We find that ERA5 and CMIP6 overestimate the magnitude of f_{sLCC} and f_{snow} in both hemisphere's mid-to-high latitudes when
compared to CloudSat-CALIPSO. In contrast, McIlhattan et al. (2017) showed that the CESM-LE underestimates the f_{LCC} by
$\sim 17\%$ and overestimates the f_{snow} by $\sim 57\%$ in the Arctic. However, since we utilize a different metric (sLCC instead of
LCC), there is no reason to expect the model biases to be identical. Furthermore, McIlhattan et al. (2017) considered a single
ESM, while here we consider an ensemble of CMIP6 models. Nevertheless, the study by McIlhattan et al. (2017) serves as
455 relevant context for our finding that ERA5 and the CMIP6 model mean produce sLCCs more frequently than observed in the
NH and SH mid-to-high latitudes, especially over the sea ice and land depending on the season (Figs. C1 and C2). In these
regions, not only is the frequency of occurrence of sLCCs too high, but the sLCCs are too efficient at producing snowfall in
ERA5 and CMIP6 models (Figs. 5 and 6). The latter finding is consistent with the findings of McIlhattan et al. (2017) that
LCCs produce snow too frequently in the CESM-LE model.

460 McIlhattan et al. (2017) explained the overestimation of f_{snow} from LCC by exploring one potential microphysical pathway
for removing supercooled cloud liquid - the WBF process. An overactive WBF process and subsequent removal of cloud ice
from the cloud through snow formation in ERA5 and CMIP6 models could also explain the large overestimation of f_{sLCC} and
f_{snow} in ERA5 and the CMIP6 model mean. ERA5 and CMIP6 models may thus have more frequent but lighter snowfall events
that lead to a higher f_{snow} while maintaining the clouds longer, compared to the CloudSat-CALIPSO observations. However,
465 for some ESMs, there is no explicit simulation of the WBF process, but rather a simple temperature-dependent partitioning of
cloud condensate into liquid and ice. For such crude parameterization schemes the identified biases are inevitable, as clouds
at a given mixed-phase temperature would always have some liquid present (hence a very high f_{sLCC}) and at the same time
always have ice available that could be converted to snow (hence a very high f_{snow}).

The difference in simulated f_{sLCC} and f_{snow} compared to CloudSat-CALIPSO in the NH and SH could, in theory, result from
470 differences in surface conditions and/or weather patterns, and thereby differences in moisture availability for the formation of
sLCCs (McIlhattan et al., 2017). However, the fact that very similar biases are found in the reanalysis as in the CMIP6 models
indicates that this is not the explanation for the identified biases, as weather patterns and surface conditions in ERA5 should

be very close to the observed. This is an important conclusion that is possible because both ERA5 and CMIP6 models were included in the present analysis. However, we cannot rule out a modest contribution to the biases from circulation differences,
475   even for the reanalysis. For example, according to Boisvert et al. (2020), all reanalysis products show lower precipitation amounts in the southern Ross Sea and Weddell Sea embayments near the ice shelves. They explain that this is due to persistent cold and dry katabatic wind blowing from the continent across the ice shelves and out over the sea ice, which is not beneficial for precipitation formation and not captured well by the reanalyses.

Under the assumption that the overall weather patterns and surface conditions are accurate in ERA5, the most plausible root
480   cause of the biases in f_{sLCC} and f_{snow} are linked to the microphysical parametrizations in the reanalysis and ESMs (Kiszler et al., 2023).

Boisvert et al. (2020) suggests that the difference in temperature and temperature threshold among various reanalysis microphysical products may explain the latitudinal inequality in snowfall amount observed between CloudSat and the reanalysis products. But here, no strong latitudinal dependence is observed in Fig. 6 as we investigate f_{snow} instead of snowfall amount.
485   The same principle should apply to ERA5 and the CMIP6 models as they rely on microphysical parametrizations. Figs. 4 and 8 show some models performing better than others for f_{sLCC} and f_{snow} in comparison to CloudSat-CALIPSO. As discussed above, many models have a simple temperature-dependent cloud phase that would almost certainly cause them to overestimate the f_{sLCC} and f_{snow}. The study by Che et al. (in prep.) investigates the supercooled-liquid fraction by isotherm for mixed-phase clouds of several CMIP6 models. They show that some of the CMIP6 models have a more variable SLF in time and space (e.g.,
490   AWI-ESM-1-1-LR, MPI-ESM1-2-LR), which might be an indication that they could have more sophisticated microphysics and could therefore, perform better in terms of sLCC and surface snowfall occurrence. Imura and Michibata (2022) studied the effect of changing the microphysical parametrization scheme from the traditional diagnostic scheme used in MIROC6, participating in CMIP6, to a prognostic scheme. They found that the prognostic scheme improved cloud coverage and snowfall in the Arctic. In our study, MIROC6 is one of the models with the largest overestimation of f_{sLCC} in the SH and the model with
495   the smallest absolute difference in boreal spring (Fig. 4). Furthermore, MIROC6, with the diagnostic scheme used here, has a large absolute difference in f_{snow} ($45\% - 60\%$) independent of hemisphere and season (Fig. 8). However, the MIROC6 with the prognostic parametrization scheme in Imura and Michibata (2022) produced light snowfall too frequently, in agreement with the results presented here, despite the use of a different microphysical scheme.

ERA5 and the CMIP6 model mean are not able to reproduce f_{snow} in comparison to CloudSat-CALIPSO. The overestimation
500   in ERA5 could be related to the global average wet bias of up to $0.27 \mathrm{mmday}^{-1}$ in the ECMWF product used in ERA5 (Lavers et al., 2021). If the modeled sLCCs are practically always snowing, then the sLCCs should have a shorter lifetime and subsequently have a lower f_{sLCC} than observations suggest. However, ERA5 and the CMIP6 model mean seem to have sLCCs that produce a little bit of snow all the time and, at the same time, maintain the sLCCs in the atmosphere. This bias may be the sLCC's counterpart to the "perpetual drizzle problem" that has been identified in ESMs for warm liquid clouds (Mülmenstädt
505   et al., 2020).

5.2 Implications for modeling and future projections

An overestimation of snowfall frequency can have significant effects on the Earth's radiative budget. The fact that the models seem to snow a little bit all the time instead of producing occasional heavy snowfall events, as well as periods with no snowfall, is therefore concerning. One implication is that there will be too frequent fresh snow deposited on top of the snow pack, ice
510 sheets, sea ice and land surfaces, with consequences for the surface albedo. With time, the aging snow surfaces darken due to snow/ice metamorphism processes and the deposition of absorbing aerosols (e.g., Picard et al., 2012; Carlsen et al., 2017). Continuous light snowfall in the model could thus lead to a simulated overestimation of the surface brightness, which in turn could limit sea ice melt in ESMs. Indeed, only ESMs that simulate excessive Arctic warming are able to reproduce the observed sea ice loss in recent decades (Notz and Stroeve, 2016).

515 Deficiencies in the representation of cloud ice formation and subsequent ice crystal growth and sedimentation can lead to inaccuracies in cloud and snowfall predictions and are a likely cause for the model biases found in this study. Cloud microphysical scheme development should, therefore, focus on improving these processes in order to reduce cloud phase and surface snowfall biases. A crucial factor is exploring more sophisticated schemes that consider the variability in cloud properties and the coexistence of liquid and ice phases within clouds. Additionally, ensemble modeling with varied model configurations,
520 parameterizations, and resolutions can give insight into what processes control sLCC and snowfall representation. Simulations at higher spatial and temporal resolution could potentially provide a more accurate representation of small-scale processes affecting cloud evolution and lifetime and could, in combination with in situ measurements, be used to test the validity of state-of-the-art cloud microphysics parameterizations. Ground and aircraft observations in connection with field campaigns should, therefore, be increased, especially for cloud phase, liquid and ice water content, and cloud top temperatures in regions
525 with sLCC formation. These field campaigns should also focus on the processes responsible for snowfall from these clouds.

Finally, satellite retrievals should be continuously improved to further refine our understanding of cloud and snowfall properties. The correct representation of these processes in models, evaluated with the help of satellite observations, is essential for simulations of weather and climate.

Code availability. The code used to analyze the satellite, ERA5, and CMIP6 data and to produce the figures is available via https://reliance.
530 rohub.org/5c135a7b-70bf-45f3-9895-3103e0e29c11?activetab=overview

Data availability. ERA5 meteorological parameters downloaded via the ERA5 CDS tool for daily statistics (C3S, 2020-11-12). CMIP6 model variables downloaded via ESGF-WCRP for 2006-2009 (https://esgf-node.llnl.gov/search/cmip6/). The standard CloudSat (Stephens et al., 2002) and CALIPSO (Winker et al., 2010) data products (version R05) used in this study (2B-CLDCLASS-LIDAR, 2C-SNOW-PROFILE, ECMWF-AUX) were downloaded from the CloudSat Data Processing Center's (at Cooperative Institute for Research in the
535 Atmosphere, Colorado State University, Fort Collins) website (http://www.cloudsat.cira.colostate.edu). The sea ice concentration data is from the Institute of Environmental Physics (IUP), University of Bremen, based on the ARTIST Sea Ice (ASI) algorithm (Spreen et al.,

2008). The daily data sets (Melsheimer and Spreen, 2019a, b, 2020a, b) were downloaded for the years 2007–2010 from the data publisher PANGAEA.

Appendix A: CMIP6 models and LWP calculation

540 The daily averages of the total mass of liquid water (LWP) in a grid box are calculated using the hydrostatic equation in CMIP6 models, besides the models from the modeling institute MOHC. First, isobaric pressure levels are retrieved with the individual CMIP6 hybrid sigma model formula found in Table A1. hyam and hybm represent the vertical coordinate formula term along the dimension Nlev. $\mathrm{p_{sfc}(i,j)}$ is the surface air pressure for each latitude (i) and longitude (j) grid box, and $\mathrm{p_0(Nlev)}$ the vertical coordinate formula term: reference pressure, both in Pa for the individual model. For CMIP6 models with orographic vertical

545 coordinates (UKESM1-0-LL, HadGEM3-GC31-LL, Table A1), represent $\mathrm{bm(Nlev)}$ the vertical coordinate formula term and $\mathrm{orog(i,j)}$ the surface altitude in units of metre.

After retrieving the pressure coordinate on half isobaric pressure levels ($\mathrm{p(i,j,Nlev-(k\pm{}^1\!/_2))}$) and $\mathrm{clw(i,j,Nlev)}$ on the full isobaric pressure levels (Nlev) in CMIP6 the lwp in each vertical grid box can be calculated with the hydrostatic equation.

$$\frac{\Delta p}{\Delta Z} = -\rho_{air}(i,j,Nlev) \cdot g$$

550 $\rho_{\mathrm{air}}(\mathrm{i,j,Nlev})$ is the density of the air mass at full isobaric pressure level. ΔZ depicts the height difference between the half isobaric pressure levels, and $\mathrm{g} = 9.81\mathrm{ms^{-2}}$ is the gravity acceleration. After the AMS Glossary of Meteorology the $\mathrm{lwp(i,j,Nlev)}$ is defined as

$$lwp(i,j,Nlev) = \int_{z=0}^{\infty} \rho_{air}(i,j,Nlev) \cdot clw(i,j,Nlev) \cdot dz = \int_{0}^{p=p_0} \rho_{air}(i,j,Nlev) \cdot clw(i,j,Nlev) \cdot \left(-\frac{dp}{\rho_{air} \cdot g}\right)$$

$$lwp(i,j,Nlev) = \int_{p=p(i,j,Nlev-(k-^1\!/_2))}^{p=p\left(i,j,Nlev-(k+^1\!/_2)\right)} \frac{clw(i,j,Nlev)}{g} \cdot dp$$

555 The LWP(i,j) can then be calculated by summing the individual $\mathrm{lwp(i,j,Nlev)}$ per vertical grid box from the surface to the top of the atmosphere. And it follows for the daily mean total liquid water path per column air in each pixel:

$$LWP(i,j) = \sum_{k=0}^{NLEV+1} lwp(i,j,Nlev) \tag{A1}$$

$$= -\frac{1}{g} \sum_{k=0}^{NLEV+1} clw(i,j,Nlev) \cdot \left[p\left(i,j,Nlev-(k-^1\!/_2)\right) - p\left(i,j,Nlev-(k+^1\!/_2)\right) \right] \tag{A2}$$

Table A1. This study uses the Coupled Model Intercomparison Phase 6 (CMIP6) models. Models marked with an asterisk ($*$) have some *historical* simulations only until 2009. Isobaric levels are calculated with a formula given by the individual model. The three equations used are ($\otimes$) $p(i,j,Nlev) = hyam(Nlev) \cdot p_0 + hybm(Nlev) \cdot p_{sfc}(i,j)$, ($\bigcirc$) $p(i,j,Nlev) = hyam(Nlev) \cdot p_0 + hybm(Nlev) \cdot p_{sfc}(i,j)$, ($\triangle$) $z(i,j,Nlev) = am(Nlev) + bm(Nlev) \cdot orog(i,j)$. Further description of the ESMs is available on the ES-DOC interface (https://explore.es-doc.org/cmip6/models/ last accessed 25. Oct 2023).

Institution	Model Name	Nom. Res.	Levels	Top level	Atmosphere	Variant	Reference
MIROC	$\otimes$ MIROC6	250km	81	0.004hPa	CCSR AGCM	r1i1p1f1	Tatebe et al. (2019)
CCCma	$\bigcirc$ CanESM5	500km	49	1hPa	CanAM5	r1i1p2f1	Swart et al. (2019)
AWI	$\bigcirc$ AWI-ESM-1-1-LR	250km	47	80km	ECHAM6.3.04p1	r1i1p1f1	Ackermann et al. (2020)
MPI-M	$\bigcirc$ MPI-ESM1-2-LR	250km	47	0.01hPa	ECHAM6.3	r1i1p1f1	Mauritsen et al. (2019)
MOHC	$\triangle$ UKESM1-0-LL	250km	85	85km	MetUM-HadGEM3-GA7.1	r5i1p1f3	Sellar et al. (2019)
MOHC	$\triangle$ HadGEM3-GC31-LL	250km	85	85km	MetUM-HadGEM3-GA7.1	r5i1p1f3	Roberts et al. (2019)
CNRM-CERFACS	$\bigcirc$ CNRM-CM6-1 *	250km	91	78.4km	Arpege 6.3	r2i1p1f2	Voldoire et al. (2019)
CNRM-CERFACS	$\bigcirc$ CNRM-ESM2-1*	250km	91	78.4km	Arpege 6.3	r1i1p1f2	Séférian et al. (2019)
IPSL	$\bigcirc$ IPSL-CM6A-LR*	250km	79	40km	LMDZ	r1i1p1f1	Boucher et al. (2020)
IPSL	$\bigcirc$ IPSL-CM5A2-INCA*	500km	39	80km	LMDZ	r1i1p1f1	Sepulchre et al. (2020)

Appendix B: Variable Unit Transformation

To compare ERA5 and CMIP6 snowfall ($\mathrm{kgm^{-2}h^{-1}}$, Table 1) to CloudSat-CALIPSO ($\mathrm{sf_{CC}}$, we apply the following multiplication to achieve the satellite surface snowfall rate in $\mathrm{mmh^{-1}}$ (Table 1). The density of water (ρ_{water}) is about 1000 kg m^{-3} and 1000 mm are one metre.

$$\mathrm{sf_{CC}} = \frac{mm}{h} \cdot \frac{1m}{1000mm} \cdot \rho_{water} = \frac{m}{h} \cdot \frac{1000kg}{1000m^3} = \frac{kg}{m^2h} \tag{B1}$$

In the ERA5 reanalysis data, the daily mean of msr has units of $\mathrm{kgm^{-2}s^{-1}}$ (Table 1). To make ERA5 snowfall daily means comparable to CloudSat and CMIP6 snowfall rate, we apply the following multiplication to achieve the mean snowfall rate per hour (msr), where we know that one hour has 3600 seconds.

$$\mathrm{sf_{ERA}} = \frac{kg}{m^2s} \cdot \frac{3600s}{h} = \frac{kg}{m^2h} \cdot 3600 \tag{B2}$$

The same is done for the CMIP6 snowfall flux parameter (prsn, Table 1).

$$\mathrm{sf_{CMIP6}} = \frac{kg}{m^2s} \cdot \frac{3600s}{h} = \frac{kg}{m^2h} \cdot 3600 \tag{B3}$$

Appendix C: Spatial distribution of f_{sLCC} and f_{snow}
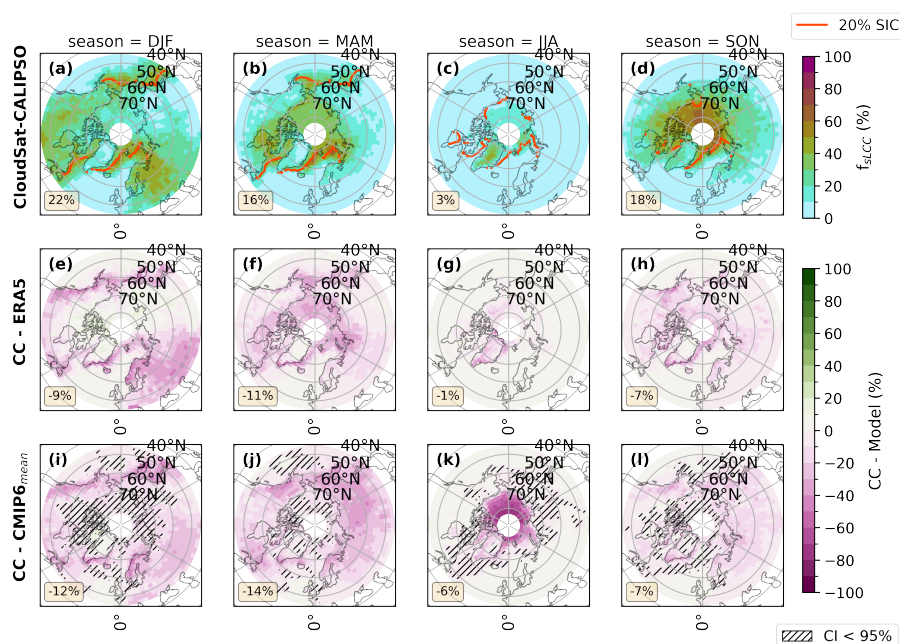
Figure C1. Seasonal averages of f_{sLCC} in the NH mid-to-high latitudes between 2007 and 2010. Combined CloudSat and CALIPSO observations are shown in the first row (a-d). The last two rows are the difference plot. They are CloudSat-CALIPSO (CC) observations minus ERA5 (e-h) or CMIP6 model mean (i-l) where valid data occurs, with green (pink) values showing underestimation (overestimation) in ERA5 and the CMIP6 model mean concerning the satellite observations. Areas, where the difference between CloudSat-CALIPSO and CMIP6 model mean is not significant ($< 95\%$) are marked with hatches. The area-weighted averages for the study area where CloudSat-CALIPSO has observations are displayed in the lower-left corner of each map. The red line (in a-d) shows the average sea ice edge of 20% sea ice concentration (SIC) between 2007 and 2010, for the given season.
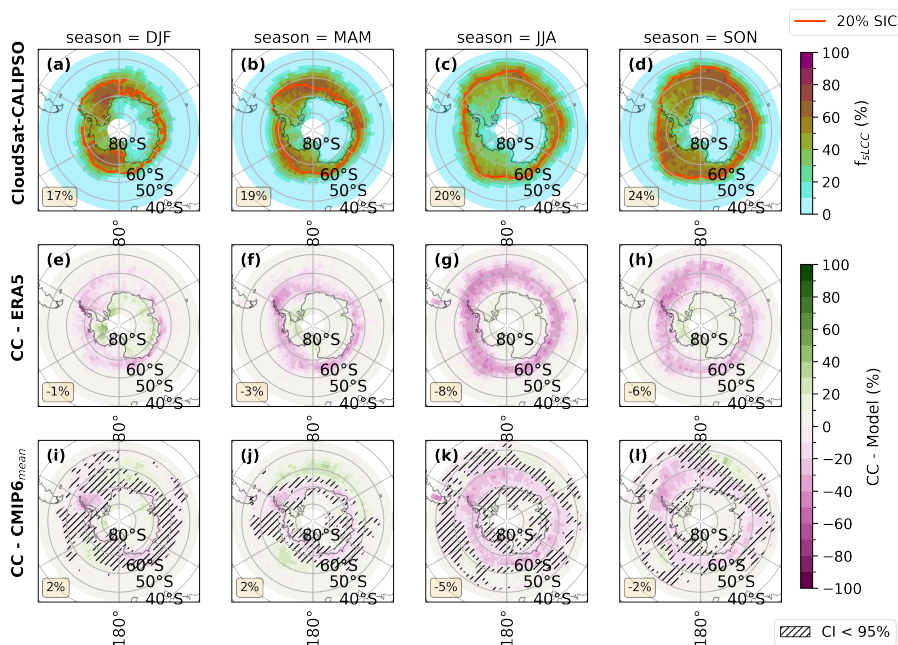
Figure C2. Seasonal averages of f_{sLCC} in the SH mid-to-high latitudes. Layout and differences are identical to Figure C1
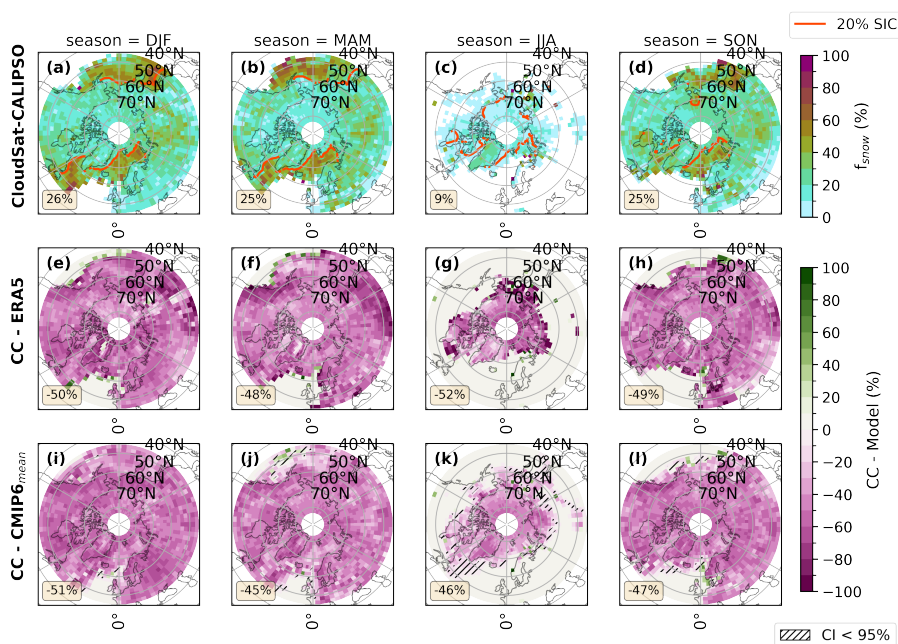
Figure C3. The figure presents the seasonal average of f_{snow} in the NH. The layout and presentation resemble Figure C1.
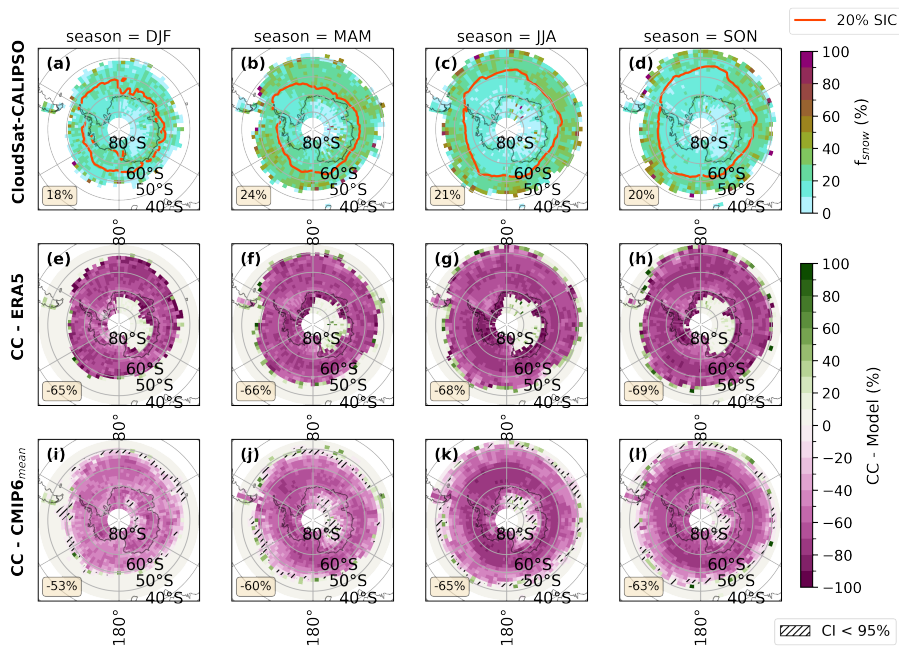
Figure C4. Seasonal averages of f_{snow} in the SH. The layout and presentation resemble Figure C1.

Appendix D: LWP threshold sensitivity - SH
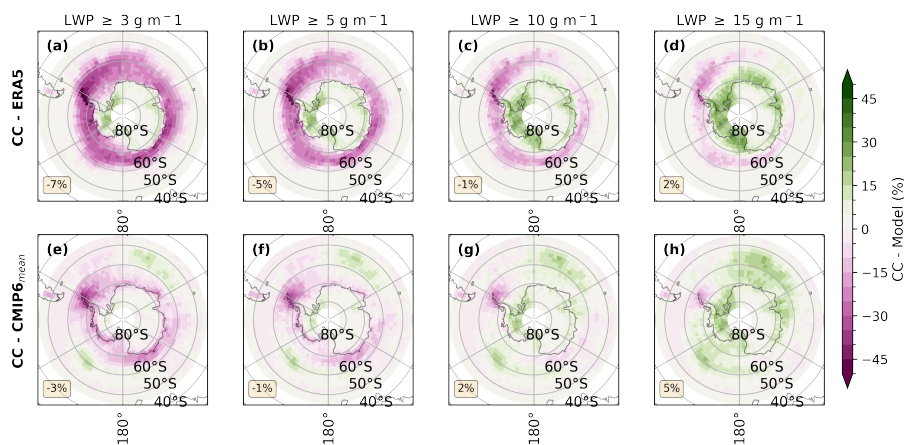
Figure D1. Annual average difference plots (CloudSat-CALIPSO (CC) minus model) for f_{sLCC} in the SH mid-to-high latitudes. The first row represents ERA5 data (a-d), and the second row shows the CMIP6 model mean (e-h) difference. LWP thresholds applied of $3\mathrm{gm}^{-2}$ (a, e), $5\mathrm{gm}^{-2}$ (b, f), $10\mathrm{gm}^{-2}$ (c, g), and $15\mathrm{gm}^{-2}$ (d, h). The analysis in this study focuses on the LWP threshold of $5\mathrm{gm}^{-2}$. The maps in each row are accompanied by area-weighted averages for the study area, located in the lower-left corner of each map. The layout and area-weighted averages are calculated the same as those in Fig. 10.

Author contributions. F.H., T.S., and A.S.D. designed the study. T.C. provided the satellite data and wrote parts of the Methods. F.H. down-loaded the ERA5 and CMIP6 data, analyzed the satellite, ERA5, and CMIP6 data, and wrote the manuscript. T.S. and A.S.D. supervised the project. T.S. provided the funding. All authors commented on several versions of the manuscript.

575 *Competing interests.* The authors declare that they have no conflict of interest.

Acknowledgements. This project has received funding from the European Research Council (ERC) under the European Union's Horizon 2020, and Horizon Europe research and innovation programs (Grant agreement numbers StG 758005 and CoG 101045273), and analyses were performed with the help of resources provided by Sigma2 - the National Infrastructure for High-Performance Computing and Data Storage in Norway. The color scheme for the scientific figures is used via the tool provided by Crameri (2018). A.S.D. work is part of the
580 ACCEPT project funded by the Norwegian Research Council. R.O.D. would also like to acknowledge EEARO-NO-2019-0423/IceSafari, contract no. 31/2020, and EU Horizon Europe research and innovation programme under grant agreement #101079385 for financial support. The authors thank Tristan L'Ecuyer, David Henderson, and Elin McIlhattan for their valuable discussions on processing the CloudSat-CALIPSO data.

References

Ackermann, L., Danek, C., Gierz, P., and Lohmann, G.: AMOC Recovery in a Multicentennial Scenario Using a Coupled Atmosphere-Ocean-Ice Sheet Model, Geophysical Research Letters, 47, e2019GL086 810, https://doi.org/10.1029/2019GL086810, _eprint: https://onlinelibrary.wiley.com/doi/pdf/10.1029/2019GL086810, 2020.

Barnett, T. P., Adam, J. C., and Lettenmaier, D. P.: Potential impacts of a warming climate on water availability in snow-dominated regions, Nature, 438, 303–309, https://doi.org/10.1038/nature04141, 2005.

Bennartz, R., Shupe, M. D., Turner, D. D., Walden, V. P., Steffen, K., Cox, C. J., Kulie, M. S., Miller, N. B., and Pettersen, C.: July 2012 Greenland melt extent enhanced by low-level liquid clouds, Nature, 496, 83–86, https://doi.org/10.1038/nature12002, number: 7443 Publisher: Nature Publishing Group, 2013.

Bergeron, T.: Über die dreidimensional verknüpfende Wetteranalyse, Norske Videnskabs Akademie, Oslo, google-Books-ID: LivKcQAA-CAAJ, 1928.

Bjordal, J., Storelvmo, T., Alterskjær, K., and Carlsen, T.: Equilibrium climate sensitivity above 5 °C plausible due to state-dependent cloud feedback, Nat. Geosci., 13, 718–721, https://doi.org/10.1038/s41561-020-00649-1, number: 11 Publisher: Nature Publishing Group, 2020.

Bodas-Salcedo, A., Webb, M. J., Bony, S., Chepfer, H., Dufresne, J.-L., Klein, S. A., Zhang, Y., Marchand, R., Haynes, J. M., Pincus, R., and John, V. O.: COSP: Satellite simulation software for model assessment, Bulletin of the American Meteorological Society, 92, 1023–1043, https://doi.org/10.1175/2011BAMS2856.1, publisher: American Meteorological Society Section: Bulletin of the American Meteorological Society, 2011.

Boisvert, L. N., Webster, M. A., Petty, A. A., Markus, T., Bromwich, D. H., and Cullather, R. I.: Intercomparison of Precipitation Estimates over the Arctic Ocean and Its Peripheral Seas from Reanalyses, Journal of Climate, 31, 8441–8462, https://doi.org/10.1175/JCLI-D-18-0125.1, publisher: American Meteorological Society Section: Journal of Climate, 2018.

Boisvert, L. N., Webster, M. A., Petty, A. A., Markus, T., Cullather, R. I., and Bromwich, D. H.: Intercomparison of Precipitation Estimates over the Southern Ocean from Atmospheric Reanalyses, Journal of Climate, 33, 10 627–10 651, https://doi.org/10.1175/JCLI-D-20-0044.1, publisher: American Meteorological Society Section: Journal of Climate, 2020.

Boucher, O., Servonnat, J., Albright, A. L., Aumont, O., Balkanski, Y., Bastrikov, V., Bekki, S., Bonnet, R., Bony, S., Bopp, L., Braconnot, P., Brockmann, P., Cadule, P., Caubel, A., Cheruy, F., Codron, F., Cozic, A., Cugnet, D., D'Andrea, F., Davini, P., de Lavergne, C., Denvil, S., Deshayes, J., Devilliers, M., Ducharne, A., Dufresne, J.-L., Dupont, E., Éthé, C., Fairhead, L., Falletti, L., Flavoni, S., Foujols, M.-A., Gardoll, S., Gastineau, G., Ghattas, J., Grandpeix, J.-Y., Guenet, B., Guez, Lionel, E., Guilyardi, E., Guimberteau, M., Hauglustaine, D., Hourdin, F., Idelkadi, A., Joussaume, S., Kageyama, M., Khodri, M., Krinner, G., Lebas, N., Levavasseur, G., Lévy, C., Li, L., Lott, F., Lurton, T., Luyssaert, S., Madec, G., Madeleine, J.-B., Maignan, F., Marchand, M., Marti, O., Mellul, L., Meurdesoif, Y., Mignot, J., Musat, I., Ottlé, C., Peylin, P., Planton, Y., Polcher, J., Rio, C., Rochetin, N., Rousset, C., Sepulchre, P., Sima, A., Swingedouw, D., Thiéblemont, R., Traore, A. K., Vancoppenolle, M., Vial, J., Vialard, J., Viovy, N., and Vuichard, N.: Presentation and Evaluation of the IPSL-CM6A-LR Climate Model, Journal of Advances in Modeling Earth Systems, 12, e2019MS002 010, https://doi.org/10.1029/2019MS002010, _eprint: https://onlinelibrary.wiley.com/doi/pdf/10.1029/2019MS002010, 2020.

Bruno, O., Hoose, C., Storelvmo, T., Coopman, Q., and Stengel, M.: Exploring the Cloud Top Phase Partitioning in Different Cloud Types Using Active and Passive Satellite Sensors, Geophysical Research Letters, 48, e2020GL089 863, https://doi.org/10.1029/2020GL089863, _eprint: https://onlinelibrary.wiley.com/doi/pdf/10.1029/2020GL089863, 2021.

620 C3S, E.: Daily statistics calculated from ERA5 data, Tech. rep., Copernicus Climate Change Service, https://cds.climate.copernicus.eu/apps/
     user-apps/app-c3s-daily-era5-statistics, 2020-11-12.

Carlsen, T. and David, R. O.: Spaceborne Evidence That Ice-Nucleating Particles Influence High-Latitude Cloud
     Phase, Geophysical Research Letters, 49, e2022GL098 041, https://doi.org/10.1029/2022GL098041, _eprint:
     https://onlinelibrary.wiley.com/doi/pdf/10.1029/2022GL098041, 2022.

625 Carlsen, T., Birnbaum, G., Ehrlich, A., Freitag, J., Heygster, G., Istomina, L., Kipfstuhl, S., Orsi, A., Schäfer, M., and Wendisch, M.:
     Comparison of different methods to retrieve optical-equivalent snow grain size in central Antarctica, The Cryosphere, 11, 2727–2741,
     https://doi.org/10.5194/tc-11-2727-2017, publisher: Copernicus GmbH, 2017.

Cesana, G., Kay, J. E., Chepfer, H., English, J. M., and de Boer, G.: Ubiquitous low-level liquid-containing Arctic clouds: New observa-
     tions and climate model constraints from CALIPSO-GOCCP, Geophysical Research Letters, 39, https://doi.org/10.1029/2012GL053385,
630 _eprint: https://onlinelibrary.wiley.com/doi/pdf/10.1029/2012GL053385, 2012.

Cesana, G., Waliser, D. E., Jiang, X., and Li, J.-L. F.: Multimodel evaluation of cloud phase transition using satellite and re-
     analysis data, Journal of Geophysical Research: Atmospheres, 120, 7871–7892, https://doi.org/10.1002/2014JD022932, _eprint:
     https://onlinelibrary.wiley.com/doi/pdf/10.1002/2014JD022932, 2015.

Che, H., Storelvmo, T., and more: Example title, in prep.

635 Chen, H., Sun, J., and Lin, W.: Anthropogenic influence would increase intense snowfall events over parts of the Northern Hemisphere in the
     future, Environ. Res. Lett., 15, 114 022, https://doi.org/10.1088/1748-9326/abbc93, publisher: IOP Publishing, 2020.

Costa, A., Meyer, J., Afchine, A., Luebke, A., Günther, G., Dorsey, J. R., Gallagher, M. W., Ehrlich, A., Wendisch, M., Baumgardner, D.,
     Wex, H., and Krämer, M.: Classification of Arctic, midlatitude and tropical clouds in the mixed-phase temperature regime, Atmos. Chem.
     Phys., 2017.

640 Crameri, F.: Scientific colour maps, https://doi.org/10.5281/zenodo.8409685, 2018.

Cucchi, M., Amici, A., Mavel, V., Bergeron, C., Brookshaw, A., Comyn-Platt, E., and Cagnazzo, C.: Daily statistics calculated
     from ERA5 data, https://datastore.copernicus-climate.eu/documents/app-c3s-daily-era5-statistics/C3S_Application-Documentation_
     ERA5-daily-statistics-v2.pdf, 2021.

Daloz, A. S., Mateling, M., L'Ecuyer, T., Kulie, M., Wood, N. B., Durand, M., Wrzesien, M., Stjern, C. W., and Dimri, A. P.: How much
645 snow falls in the world's mountains? A first look at mountain snowfall estimates in A-train observations and reanalyses, The Cryosphere
     Discussions, pp. 1–23, https://doi.org/https://doi.org/10.5194/tc-2019-302, publisher: Copernicus GmbH, 2020.

Danco, J. F., DeAngelis, A. M., Raney, B. K., and Broccoli, A. J.: Effects of a Warming Climate on Daily Snowfall Events in the Northern
     Hemisphere, Journal of Climate, 29, 6295–6318, https://doi.org/10.1175/JCLI-D-15-0687.1, publisher: American Meteorological Society
     Section: Journal of Climate, 2016.

650 Dee, D. P., Uppala, S. M., Simmons, A. J., Berrisford, P., Poli, P., Kobayashi, S., Andrae, U., Balmaseda, M. A., Balsamo, G., Bauer, P.,
     Bechtold, P., Beljaars, A. C. M., van de Berg, L., Bidlot, J., Bormann, N., Delsol, C., Dragani, R., Fuentes, M., Geer, A. J., Haimberger, L.,
     Healy, S. B., Hersbach, H., Hólm, E. V., Isaksen, L., Kållberg, P., Köhler, M., Matricardi, M., McNally, A. P., Monge-Sanz, B. M., Mor-
     crette, J.-J., Park, B.-K., Peubey, C., de Rosnay, P., Tavolato, C., Thépaut, J.-N., and Vitart, F.: The ERA-Interim reanalysis: configuration
     and performance of the data assimilation system, Q.J.R. Meteorol. Soc., 137, 553–597, https://doi.org/10.1002/qj.828, 2011.

655 DeMott, P. J., Prenni, A. J., Liu, X., Kreidenweis, S. M., Petters, M. D., Twohy, C. H., Richardson, M. S., Eidhammer, T., and Rogers, D. C.:
     Predicting global atmospheric ice nuclei distributions and their impacts on climate, Proceedings of the National Academy of Sciences,
     107, 11 217–11 222, https://doi.org/10.1073/pnas.0910818107, publisher: Proceedings of the National Academy of Sciences, 2010.

Douville, H., Raghavan, K., Renwick, J., Allan, R., Arias, P., Barlow, M., Cerezo-Mota, R., Cherchi, A., Gan, T., Gergis, J., Jiang, D., Khan, A., Pokam Mba, W., Rosenfeld, D., Tierney, J., and Zolina, O.: Chapter 8: Water Cycle Changes, in: In Climate Change 2021: The Physical Science Basis. Contribution of Working Group I to the Sixth Assessment Report of the Intergovernmental Panel on Climate Change [Masson-Delmotte, V., P. Zhai, A. Pirani, S.L. Connors, C. Péan, S. Berger, N. Caud, Y. Chen, L. Goldfarb, M.I. Gomis, M. Huang, K. Leitzell, E. Lonnoy, J.B.R. Matthews, T.K. Maycock, T. Waterfield, O. Yelekçi, R. Yu, and B. Zhou (eds.)]., pp. 1055–1210, Cambridge University Press, Cambridge, United Kingdom and New York, NY, USA, ISBN 978-1-00-915788-9, https://doi.org/10.1017/9781009157896.010, 2023.

Edel, L., Claud, C., Genthon, C., Palerme, C., Wood, N., L'Ecuyer, T., and Bromwich, D.: Arctic Snowfall from CloudSat Observations and Reanalyses, Journal of Climate, 33, 2093–2109, https://doi.org/10.1175/JCLI-D-19-0105.1, publisher: American Meteorological Society Section: Journal of Climate, 2020.

Ehrlich, A., Wendisch, M., Bierwirth, E., and Mainz, J. G.-U.: Evidence of ice crystals at cloud top of Arctic boundary-layer mixed-phase clouds derived from airborne remote sensing, Atmos. Chem. Phys., 2009.

Eisenberg, D. and Warner, K. E.: Effects of Snowfalls on Motor Vehicle Collisions, Injuries, and Fatalities, Am J Public Health, 95, 120–124, https://doi.org/10.2105/AJPH.2004.048926, publisher: American Public Health Association, 2005.

Eyring, V., Bony, S., Meehl, G. A., Senior, C. A., Stevens, B., Stouffer, R. J., and Taylor, K. E.: Overview of the Coupled Model Intercomparison Project Phase 6 (CMIP6) experimental design and organization, Geosci. Model Dev., 9, 1937–1958, https://doi.org/10.5194/gmd-9-1937-2016, 2016.

Findeisen, W.: Colloidal meteorological processes in the formation of precipitation, Meteorologische Zeitschrift, pp. 443–454, https://doi.org/10.1127/metz/2015/0675, publisher: Schweizerbart'sche Verlagsbuchhandlung, 2015.

Fletcher, J. K., Mason, S., and Jakob, C.: A Climatology of Clouds in Marine Cold Air Outbreaks in Both Hemispheres, Journal of Climate, 29, 6677–6692, https://doi.org/10.1175/JCLI-D-15-0783.1, publisher: American Meteorological Society Section: Journal of Climate, 2016.

Forbes, R. and Tompkins, A.: An improved representation of cloud and precipitation, ECMWF Newsletter, https://doi.org/10.21957/NFGULZHE, publisher: ECMWF, 2011.

Forbes, R., Tompkins, A., and Untch, A.: A new prognostic bulk microphysics scheme for the IFS, ECMWF Technical Memorandum, 649, https://www.ecmwf.int/sites/default/files/elibrary/2011/9441-new-prognostic-bulk-microphysics-scheme-ifs.pdf, 2011.

Forbes, R. M. and Ahlgrimm, M.: On the Representation of High-Latitude Boundary Layer Mixed-Phase Cloud in the ECMWF Global Model, Monthly Weather Review, 142, 3425–3445, https://doi.org/10.1175/MWR-D-13-00325.1, publisher: American Meteorological Society Section: Monthly Weather Review, 2014.

Fox, S., Crawford, A., McCrystall, M., Stroeve, J., Lukovich, J., Loeb, N., Natanine, J., and Serreze, M.: Extreme Arctic Weather and Community Impacts in Nunavut: A Case Study of One Winter's Storms and Lessons for Local Climate Change Preparedness, Weather, Climate, and Society, 15, 881–892, https://doi.org/10.1175/WCAS-D-23-0006.1, publisher: American Meteorological Society Section: Weather, Climate, and Society, 2023.

Geerts, B., Giangrande, S. E., McFarquhar, G. M., Xue, L., Abel, S. J., Comstock, J. M., Crewell, S., DeMott, P. J., Ebell, K., Field, P., Hill, T. C. J., Hunzinger, A., Jensen, M. P., Johnson, K. L., Juliano, T. W., Kollias, P., Kosovic, B., Lackner, C., Luke, E., Lüpkes, C., Matthews, A. A., Neggers, R., Ovchinnikov, M., Powers, H., Shupe, M. D., Spengler, T., Swanson, B. E., Tjernström, M., Theisen, A. K., Wales, N. A., Wang, Y., Wendisch, M., and Wu, P.: The COMBLE Campaign: A Study of Marine Boundary Layer Clouds in Arctic Cold-Air

695   Outbreaks, Bulletin of the American Meteorological Society, 103, E1371–E1389, https://doi.org/10.1175/BAMS-D-21-0044.1, publisher: American Meteorological Society Section: Bulletin of the American Meteorological Society, 2022.

Henderson, D. S., L'Ecuyer, T., Stephens, G., Partain, P., and Sekiguchi, M.: A Multisensor Perspective on the Radiative Impacts of Clouds and Aerosols, Journal of Applied Meteorology and Climatology, 52, 853–871, https://doi.org/10.1175/JAMC-D-12-025.1, publisher: American Meteorological Society Section: Journal of Applied Meteorology and Climatology, 2013.

700   Hersbach, H., Bell, B., Berrisford, P., Hirahara, S., Horányi, A., Muñoz-Sabater, J., Nicolas, J., Peubey, C., Radu, R., Schepers, D., Simmons, A., Soci, C., Abdalla, S., Abellan, X., Balsamo, G., Bechtold, P., Biavati, G., Bidlot, J., Bonavita, M., De Chiara, G., Dahlgren, P., Dee, D., Diamantakis, M., Dragani, R., Flemming, J., Forbes, R., Fuentes, M., Geer, A., Haimberger, L., Healy, S., Hogan, R. J., Hólm, E., Janisková, M., Keeley, S., Laloyaux, P., Lopez, P., Lupu, C., Radnoti, G., de Rosnay, P., Rozum, I., Vamborg, F., Villaume, S., and Thépaut, J.-N.: The ERA5 global reanalysis, Quarterly Journal of the Royal Meteorological Society, 146, 1999–2049,
705   https://doi.org/10.1002/qj.3803, _eprint: https://rmets.onlinelibrary.wiley.com/doi/pdf/10.1002/qj.3803, 2020.

Heymsfield, A. J., Schmitt, C., Chen, C.-C.-J., Bansemer, A., Gettelman, A., Field, P. R., and Liu, C.: Contributions of the Liquid and Ice Phases to Global Surface Precipitation: Observations and Global Climate Modeling, Journal of the Atmospheric Sciences, 77, 2629–2648, https://doi.org/10.1175/JAS-D-19-0352.1, publisher: American Meteorological Society Section: Journal of the Atmospheric Sciences, 2020.

710   Hiley, M. J., Kulie, M. S., and Bennartz, R.: Uncertainty Analysis for CloudSat Snowfall Retrievals, Journal of Applied Meteorology and Climatology, 50, 399–418, https://doi.org/10.1175/2010JAMC2505.1, publisher: American Meteorological Society Section: Journal of Applied Meteorology and Climatology, 2011.

Hofer, S., Tedstone, A. J., Fettweis, X., and Bamber, J. L.: Cloud microphysics and circulation anomalies control differences in future Greenland melt, Nat. Clim. Chang., 9, 523–528, https://doi.org/10.1038/s41558-019-0507-8, number: 7 Publisher: Nature Publishing
715   Group, 2019.

Imura, Y. and Michibata, T.: Too Frequent and Too Light Arctic Snowfall With Incorrect Precipitation Phase Partitioning in the MIROC6 GCM, Journal of Advances in Modeling Earth Systems, 14, e2022MS003 046, https://doi.org/10.1029/2022MS003046, _eprint: https://agupubs.onlinelibrary.wiley.com/doi/pdf/10.1029/2022MS003046, 2022.

Jiusto, J. E. and Weickmann, H. K.: Types of snowfall, Bulletin of the American Meteorological Society, 54, 1148–1162,
720   https://doi.org/10.1175/1520-0477(1973)054<1148:TOS>2.0.CO;2, publisher: American Meteorological Society Section: Bulletin of the American Meteorological Society, 1973.

Kay, J. E., Bourdages, L., Miller, N. B., Morrison, A., Yettella, V., Chepfer, H., and Eaton, B.: Evaluating and improving cloud phase in the Community Atmosphere Model version 5 using spaceborne lidar observations, Journal of Geophysical Research: Atmospheres, 121, 4162–4176, https://doi.org/10.1002/2015JD024699, _eprint: https://onlinelibrary.wiley.com/doi/pdf/10.1002/2015JD024699, 2016.

725   Keys, D. J.: Wilkinson Microwave Anisotropy Probe (WMAP) Battery Operations Problem Resolution Team (PRT), Tech. Rep. NF1676L-11245, NASA Goddard Space Flight Center, https://ntrs.nasa.gov/citations/20100030608, nTRS Author Affiliations: NASA Goddard Space Flight Center NTRS Document ID: 20100030608 NTRS Research Center: Langley Research Center (LaRC), 2010.

Kiszler, T., Ori, D., and Schemann, V.: Microphysical processes involving the vapour phase dominate in simulated low-level Arctic clouds, EGUsphere, pp. 1–18, https://doi.org/10.5194/egusphere-2023-2986, publisher: Copernicus GmbH, 2023.

730   Komurcu, M., Storelvmo, T., Tan, I., Lohmann, U., Yun, Y., Penner, J. E., Wang, Y., Liu, X., and Takemura, T.: Intercomparison of the cloud water phase among global climate models, Journal of Geophysical Research: Atmospheres, 119, 3372–3400, https://doi.org/10.1002/2013JD021119, 2014.

Korolev, A.: Limitations of the Wegener–Bergeron–Findeisen Mechanism in the Evolution of Mixed-Phase Clouds, Journal of the Atmospheric Sciences, 64, 3372–3375, https://doi.org/10.1175/JAS4035.1, publisher: American Meteorological Society Section: Journal of the Atmospheric Sciences, 2007.

Korolev, A. and Milbrandt, J.: How Are Mixed-Phase Clouds Mixed?, Geophysical Research Letters, 49, e2022GL099 578, https://doi.org/10.1029/2022GL099578, _eprint: https://onlinelibrary.wiley.com/doi/pdf/10.1029/2022GL099578, 2022.

Korolev, A., McFarquhar, G., Field, P. R., Franklin, C., Lawson, P., Wang, Z., Williams, E., Abel, S. J., Axisa, D., Borrmann, S., Crosier, J., Fugal, J., Krämer, M., Lohmann, U., Schlenczek, O., Schnaiter, M., and Wendisch, M.: Mixed-Phase Clouds: Progress and Challenges, Meteorological Monographs, 58, 5.1–5.50, https://doi.org/10.1175/AMSMONOGRAPHS-D-17-0001.1, publisher: American Meteorological Society Section: Meteorological Monographs, 2017.

Korolev, A. V. and Mazin, I. P.: Supersaturation of Water Vapor in Clouds, Journal of the Atmospheric Sciences, 60, 2957–2974, https://doi.org/10.1175/1520-0469(2003)060<2957:SOWVIC>2.0.CO;2, publisher: American Meteorological Society Section: Journal of the Atmospheric Sciences, 2003.

Kotarba, A. Z.: Errors in global cloud climatology due to transect sampling with the CALIPSO satellite lidar mission, Atmospheric Research, 279, 106 379, https://doi.org/10.1016/j.atmosres.2022.106379, 2022.

Kulie, M. S. and Bennartz, R.: Utilizing Spaceborne Radars to Retrieve Dry Snowfall, Journal of Applied Meteorology and Climatology, 48, 2564–2580, https://doi.org/10.1175/2009JAMC2193.1, publisher: American Meteorological Society Section: Journal of Applied Meteorology and Climatology, 2009.

Lavers, D. A., Harrigan, S., and Prudhomme, C.: Precipitation Biases in the ECMWF Integrated Forecasting System, Journal of Hydrometeorology, 22, 1187–1198, https://doi.org/10.1175/JHM-D-20-0308.1, publisher: American Meteorological Society Section: Journal of Hydrometeorology, 2021.

Lohmann, U. and Diehl, K.: Sensitivity Studies of the Importance of Dust Ice Nuclei for the Indirect Aerosol Effect on Stratiform Mixed-Phase Clouds, Journal of the Atmospheric Sciences, 63, 968–982, https://doi.org/10.1175/JAS3662.1, publisher: American Meteorological Society Section: Journal of the Atmospheric Sciences, 2006.

Mateling, M. E., Pettersen, C., Kulie, M. S., and L'Ecuyer, T. S.: Marine Cold-Air Outbreak Snowfall in the North Atlantic: A CloudSat Perspective, Journal of Geophysical Research: Atmospheres, 128, e2022JD038 053, https://doi.org/10.1029/2022JD038053, _eprint: https://onlinelibrary.wiley.com/doi/pdf/10.1029/2022JD038053, 2023.

Matus, A. V. and L'Ecuyer, T. S.: The role of cloud phase in Earth's radiation budget, Journal of Geophysical Research: Atmospheres, 122, 2559–2578, https://doi.org/10.1002/2016JD025951, 2017.

Mauritsen, T., Bader, J., Becker, T., Behrens, J., Bittner, M., Brokopf, R., Brovkin, V., Claussen, M., Crueger, T., Esch, M., Fast, I., Fiedler, S., Fläschner, D., Gayler, V., Giorgetta, M., Goll, D. S., Haak, H., Hagemann, S., Hedemann, C., Hohenegger, C., Ilyina, T., Jahns, T., Jimenéz-de-la Cuesta, D., Jungclaus, J., Kleinen, T., Kloster, S., Kracher, D., Kinne, S., Kleberg, D., Lasslop, G., Kornblueh, L., Marotzke, J., Matei, D., Meraner, K., Mikolajewicz, U., Modali, K., Möbis, B., Müller, W. A., Nabel, J. E. M. S., Nam, C. C. W., Notz, D., Nyawira, S.-S., Paulsen, H., Peters, K., Pincus, R., Pohlmann, H., Pongratz, J., Popp, M., Raddatz, T. J., Rast, S., Redler, R., Reick, C. H., Rohrschneider, T., Schemann, V., Schmidt, H., Schnur, R., Schulzweida, U., Six, K. D., Stein, L., Stemmler, I., Stevens, B., von Storch, J.-S., Tian, F., Voigt, A., Vrese, P., Wieners, K.-H., Wilkenskjeld, S., Winkler, A., and Roeckner, E.: Developments in the MPI-M Earth System Model version 1.2 (MPI-ESM1.2) and Its Response to Increasing CO2, Journal of Advances in Modeling Earth Systems, 11, 998–1038, https://doi.org/https://doi.org/10.1029/2018MS001400, 2019.

770 McIlhattan, E. A., L'Ecuyer, T. S., and Miller, N. B.: Observational Evidence Linking Arctic Supercooled Liquid Cloud Biases in CESM to Snowfall Processes, Journal of Climate, 30, 4477–4495, https://doi.org/10.1175/JCLI-D-16-0666.1, publisher: American Meteorological Society Section: Journal of Climate, 2017.

Melsheimer, C. and Spreen, G.: AMSR2 ASI sea ice concentration data, Antarctic, version 5.4 (NetCDF) (July 2012 - December 2019), https://doi.org/10.1594/PANGAEA.898400, 2019a.

775 Melsheimer, C. and Spreen, G.: AMSR2 ASI sea ice concentration data, Arctic, version 5.4 (NetCDF) (July 2012 - December 2019), https://doi.org/10.1594/PANGAEA.898399, 2019b.

Melsheimer, C. and Spreen, G.: AMSR-E ASI sea ice concentration data, Antarctic, version 5.4 (NetCDF) (June 2002 - September 2011), https://doi.org/10.1594/PANGAEA.919778, 2020a.

Melsheimer, C. and Spreen, G.: AMSR-E ASI sea ice concentration data, Arctic, version 5.4 (NetCDF) (June 2002 - September 2011),
780 https://doi.org/10.1594/PANGAEA.919777, 2020b.

Milani, L., Kulie, M. S., Casella, D., Dietrich, S., L'Ecuyer, T. S., Panegrossi, G., Porcù, F., Sanò, P., and Wood, N. B.: CloudSat snowfall estimates over Antarctica and the Southern Ocean: An assessment of independent retrieval methodologies and multi-year snowfall analysis, Atmospheric Research, 213, 121–135, https://doi.org/10.1016/j.atmosres.2018.05.015, 2018.

Murray, B. J., Carslaw, K. S., and Field, P. R.: Opinion: Cloud-phase climate feedback and the importance of ice-nucleating particles, Atmos.
785 Chem. Phys., 21, 665–679, https://doi.org/10.5194/acp-21-665-2021, 2021.

Mülmenstädt, J., Nam, C., Salzmann, M., Kretzschmar, J., L'Ecuyer, T. S., Lohmann, U., Ma, P.-L., Myhre, G., Neubauer, D., Stier, P., Suzuki, K., Wang, M., and Quaas, J.: Reducing the aerosol forcing uncertainty using observational constraints on warm rain processes, Science Advances, 6, eaaz6433, https://doi.org/10.1126/sciadv.aaz6433, publisher: American Association for the Advancement of Science, 2020.

Mülmenstädt, J., Salzmann, M., Kay, J. E., Zelinka, M. D., Ma, P.-L., Nam, C., Kretzschmar, J., Hörnig, S., and Quaas, J.: An underestimated
790 negative cloud feedback from cloud lifetime changes, Nat. Clim. Chang., 11, 508–513, https://doi.org/10.1038/s41558-021-01038-1, number: 6 Publisher: Nature Publishing Group, 2021.

Notz, D. and Stroeve, J.: Observed Arctic sea-ice loss directly follows anthropogenic CO2 emission, Science, 354, 747–750, https://doi.org/10.1126/science.aag2345, publisher: American Association for the Advancement of Science, 2016.

Papritz, L. and Sodemann, H.: Characterizing the Local and Intense Water Cycle during a Cold Air Outbreak in the Nordic Seas, Monthly
795 Weather Review, 146, 3567–3588, https://doi.org/10.1175/MWR-D-18-0172.1, publisher: American Meteorological Society Section: Monthly Weather Review, 2018.

Picard, G., Domine, F., Krinner, G., Arnaud, L., and Lefebvre, E.: Inhibition of the positive snow-albedo feedback by precipitation in interior Antarctica, Nature Clim Change, 2, 795–798, https://doi.org/10.1038/nclimate1590, publisher: Nature Publishing Group, 2012.

Proske, U., Bessenbacher, V., Dedekind, Z., Lohmann, U., and Neubauer, D.: How frequent is natural cloud seeding from ice cloud layers (
800 < -35 °C) over Switzerland?, Atmospheric Chemistry and Physics, 21, 5195–5216, https://doi.org/10.5194/acp-21-5195-2021, publisher: Copernicus GmbH, 2021.

Quante, L., Willner, S. N., Middelanis, R., and Levermann, A.: Regions of intensification of extreme snowfall under future warming, Sci Rep, 11, 16 621, https://doi.org/10.1038/s41598-021-95979-4, number: 1 Publisher: Nature Publishing Group, 2021.

Roberts, M. J., Baker, A., Blockley, E. W., Calvert, D., Coward, A., Hewitt, H. T., Jackson, L. C., Kuhlbrodt, T., Mathiot, P., Roberts, C. D.,
805 Schiemann, R., Seddon, J., Vannière, B., and Vidale, P. L.: Description of the resolution hierarchy of the global coupled HadGEM3-GC3.1 model as used in CMIP6 HighResMIP experiments, Geoscientific Model Development, 12, 4999–5028, https://doi.org/10.5194/gmd-12-4999-2019, publisher: Copernicus GmbH, 2019.

Rosenfeld, D., Yu, X., Liu, G., Xu, X., Zhu, Y., Yue, Z., Dai, J., Dong, Z., Dong, Y., and Peng, Y.: Glaciation temperatures of convective clouds ingesting desert dust, air pollution and smoke from forest fires, Geophysical Research Letters, 38, https://doi.org/10.1029/2011GL049423,
810   _eprint: https://onlinelibrary.wiley.com/doi/pdf/10.1029/2011GL049423, 2011.

Roussel, M.-L., Lemonnier, F., Genthon, C., and Krinner, G.: Brief communication: Evaluating Antarctic precipitation in ERA5 and CMIP6 against CloudSat observations, The Cryosphere, 14, 2715–2727, https://doi.org/10.5194/tc-14-2715-2020, publisher: Copernicus GmbH, 2020.

Sassen, K., Wang, Z., and Liu, D.: Global distribution of cirrus clouds from CloudSat/Cloud-Aerosol Lidar and Infrared Pathfinder Satellite
815   Observations (CALIPSO) measurements, Journal of Geophysical Research: Atmospheres, 113, https://doi.org/10.1029/2008JD009972, _eprint: https://onlinelibrary.wiley.com/doi/pdf/10.1029/2008JD009972, 2008.

Schirmacher, I., Kollias, P., Lamer, K., Mech, M., Pfitzenmaier, L., Wendisch, M., and Crewell, S.: Assessing Arctic low-level clouds and precipitation from above – a radar perspective, Atmospheric Measurement Techniques, 16, 4081–4100, https://doi.org/10.5194/amt-16-4081-2023, publisher: Copernicus GmbH, 2023.

820 Scott, D., Dawson, J., and Jones, B.: Climate change vulnerability of the US Northeast winter recreation– tourism sector, Mitig Adapt Strateg Glob Change, 13, 577–596, https://doi.org/10.1007/s11027-007-9136-z, 2008.

Sellar, A. A., Jones, C. G., Mulcahy, J. P., Tang, Y., Yool, A., Wiltshire, A., O'Connor, F. M., Stringer, M., Hill, R., Palmieri, J., Woodward, S., de Mora, L., Kuhlbrodt, T., Rumbold, S. T., Kelley, D. I., Ellis, R., Johnson, C. E., Walton, J., Abraham, N. L., Andrews, M. B., Andrews, T., Archibald, A. T., Berthou, S., Burke, E., Blockley, E., Carslaw, K., Dalvi, M., Edwards, J., Folberth, G. A., Gedney, N.,
825   Griffiths, P. T., Harper, A. B., Hendry, M. A., Hewitt, A. J., Johnson, B., Jones, A., Jones, C. D., Keeble, J., Liddicoat, S., Morgenstern, O., Parker, R. J., Predoi, V., Robertson, E., Siahaan, A., Smith, R. S., Swaminathan, R., Woodhouse, M. T., Zeng, G., and Zerroukat, M.: UKESM1: Description and Evaluation of the U.K. Earth System Model, Journal of Advances in Modeling Earth Systems, 11, 4513–4558, https://doi.org/10.1029/2019MS001739, _eprint: https://onlinelibrary.wiley.com/doi/pdf/10.1029/2019MS001739, 2019.

Sepulchre, P., Caubel, A., Ladant, J.-B., Bopp, L., Boucher, O., Braconnot, P., Brockmann, P., Cozic, A., Donnadieu, Y., Dufresne,
830   J.-L., Estella-Perez, V., Ethé, C., Fluteau, F., Foujols, M.-A., Gastineau, G., Ghattas, J., Hauglustaine, D., Hourdin, F., Kageyama, M., Khodri, M., Marti, O., Meurdesoif, Y., Mignot, J., Sarr, A.-C., Servonnat, J., Swingedouw, D., Szopa, S., and Tardif, D.: IPSL-CM5A2 – an Earth system model designed for multi-millennial climate simulations, Geoscientific Model Development, 13, 3011–3053, https://doi.org/10.5194/gmd-13-3011-2020, publisher: Copernicus GmbH, 2020.

Shaw, J., McGraw, Z., Bruno, O., Storelvmo, T., and Hofer, S.: Using Satellite Observations to Evaluate Model Microphysical Representation
835   of Arctic Mixed-Phase Clouds, Geophysical Research Letters, 49, e2021GL096 191, https://doi.org/10.1029/2021GL096191, _eprint: https://onlinelibrary.wiley.com/doi/pdf/10.1029/2021GL096191, 2022.

Shupe, M. D. and Intrieri, J. M.: Cloud Radiative Forcing of the Arctic Surface: The Influence of Cloud Properties, Surface Albedo, and Solar Zenith Angle, Journal of Climate, 17, 616–628, https://doi.org/10.1175/1520-0442(2004)017<0616:CRFOTA>2.0.CO;2, publisher: American Meteorological Society Section: Journal of Climate, 2004.

840 Shupe, M. D., Turner, D. D., Walden, V. P., Bennartz, R., Cadeddu, M. P., Castellani, B. B., Cox, C. J., Hudak, D. R., Kulie, M. S., Miller, N. B., Neely, R. R., Neff, W. D., and Rowe, P. M.: High and Dry: New Observations of Tropospheric and Cloud Properties above the Greenland Ice Sheet, Bulletin of the American Meteorological Society, 94, 169–186, https://doi.org/10.1175/BAMS-D-11-00249.1, publisher: American Meteorological Society Section: Bulletin of the American Meteorological Society, 2013.

Simmons, A., Uppala, S., Dee, D., and Kobayashi, S.: ERA-Interim: New ECMWF reanalysis products from 1989 onwards,
845   https://doi.org/10.21957/pocnex23c6, 2007.

Spreen, G., Kaleschke, L., and Heygster, G.: Sea ice remote sensing using AMSR-E 89-GHz channels, Journal of Geophysical Research: Oceans, 113, https://doi.org/10.1029/2005JC003384, _eprint: https://onlinelibrary.wiley.com/doi/pdf/10.1029/2005JC003384, 2008.

Stanford, M. W., Fridlind, A. M., Silber, I., Ackerman, A. S., Cesana, G., Mülmenstädt, J., Protat, A., Alexander, S., and McDonald, A.: Earth-system-model evaluation of cloud and precipitation occurrence for supercooled and warm clouds over the Southern Ocean's Macquarie
850   Island, Atmospheric Chemistry and Physics, 23, 9037–9069, https://doi.org/10.5194/acp-23-9037-2023, publisher: Copernicus GmbH, 2023.

Stephens, G. L. and Kummerow, C. D.: The Remote Sensing of Clouds and Precipitation from Space: A Review, Journal of the Atmospheric Sciences, 64, 3742–3765, https://doi.org/10.1175/2006JAS2375.1, publisher: American Meteorological Society Section: Journal of the Atmospheric Sciences, 2007.

855   Stephens, G. L., Vane, D. G., Boain, R. J., Mace, G. G., Sassen, K., Wang, Z., Illingworth, A. J., O'connor, E. J., Rossow, W. B., Durden, S. L., Miller, S. D., Austin, R. T., Benedetti, A., and Mitrescu, C.: The cloudsat mission and the a-train, Bull. Amer. Meteor. Soc., 83, 1771–1790, https://doi.org/10.1175/BAMS-83-12-1771, 2002.

Storelvmo, T. and Tan, I.: The Wegener-Bergeron-Findeisen process – Its discovery and vital importance for weather and climate, Meteorologische Zeitschrift, 24, 455–461, https://doi.org/10.1127/metz/2015/0626, publisher: Borntraeger, 2015.

860   Swart, N. C., Cole, J. N. S., Kharin, V. V., Lazare, M., Scinocca, J. F., Gillett, N. P., Anstey, J., Arora, V., Christian, J. R., Hanna, S., Jiao, Y., Lee, W. G., Majaess, F., Saenko, O. A., Seiler, C., Seinen, C., Shao, A., Sigmond, M., Solheim, L., von Salzen, K., Yang, D., and Winter, B.: The Canadian Earth System Model version 5 (CanESM5.0.3), Geoscientific Model Development, 12, 4823–4873, https://doi.org/10.5194/gmd-12-4823-2019, publisher: Copernicus GmbH, 2019.

Séférian, R., Nabat, P., Michou, M., Saint-Martin, D., Voldoire, A., Colin, J., Decharme, B., Delire, C., Berthet, S., Chevallier, M.,
865   Sénési, S., Franchisteguy, L., Vial, J., Mallet, M., Joetzjer, E., Geoffroy, O., Guérémy, J.-F., Moine, M.-P., Msadek, R., Ribes, A., Rocher, M., Roehrig, R., Salas-y Mélia, D., Sanchez, E., Terray, L., Valcke, S., Waldman, R., Aumont, O., Bopp, L., Deshayes, J., Éthé, C., and Madec, G.: Evaluation of CNRM Earth System Model, CNRM-ESM2-1: Role of Earth System Processes in Present-Day and Future Climate, Journal of Advances in Modeling Earth Systems, 11, 4182–4227, https://doi.org/10.1029/2019MS001791, _eprint: https://onlinelibrary.wiley.com/doi/pdf/10.1029/2019MS001791, 2019.

870   Tan, I. and Storelvmo, T.: Sensitivity Study on the Influence of Cloud Microphysical Parameters on Mixed-Phase Cloud Thermodynamic Phase Partitioning in CAM5, Journal of the Atmospheric Sciences, 73, 709–728, https://doi.org/10.1175/JAS-D-15-0152.1, publisher: American Meteorological Society Section: Journal of the Atmospheric Sciences, 2016.

Tatebe, H., Ogura, T., Nitta, T., Komuro, Y., Ogochi, K., Takemura, T., Sudo, K., Sekiguchi, M., Abe, M., Saito, F., Chikira, M., Watanabe, S., Mori, M., Hirota, N., Kawatani, Y., Mochizuki, T., Yoshimura, K., Takata, K., O'ishi, R., Yamazaki, D., Suzuki, T., Kurogi, M., Kataoka,
875   T., Watanabe, M., and Kimoto, M.: Description and basic evaluation of simulated mean state, internal variability, and climate sensitivity in MIROC6, Geoscientific Model Development, 12, 2727–2765, https://doi.org/10.5194/gmd-12-2727-2019, publisher: Copernicus GmbH, 2019.

Taylor, K. E., Stouffer, R. J., and Meehl, G. A.: An Overview of CMIP5 and the Experiment Design, Bulletin of the American Meteorological Society, 93, 485–498, https://doi.org/10.1175/BAMS-D-11-00094.1, publisher: American Meteorological Society Section: Bulletin of the
880   American Meteorological Society, 2012.

Vergara-Temprado, J., Miltenberger, A. K., Furtado, K., Grosvenor, D. P., Shipway, B. J., Hill, A. A., Wilkinson, J. M., Field, P. R., Murray, B. J., and Carslaw, K. S.: Strong control of Southern Ocean cloud reflectivity by ice-nucleating particles, Proceedings of the National

Academy of Sciences, 115, 2687–2692, https://doi.org/10.1073/pnas.1721627115, publisher: Proceedings of the National Academy of Sciences, 2018.

885 Voldoire, A., Saint-Martin, D., Sénési, S., Decharme, B., Alias, A., Chevallier, M., Colin, J., Guérémy, J.-F., Michou, M., Moine, M.-P., Nabat, P., Roehrig, R., Salas y Mélia, D., Séférian, R., Valcke, S., Beau, I., Belamari, S., Berthet, S., Cassou, C., Cattiaux, J., Deshayes, J., Douville, H., Ethé, C., Franchistéguy, L., Geoffroy, O., Lévy, C., Madec, G., Meurdesoif, Y., Msadek, R., Ribes, A., Sanchez-Gomez, E., Terray, L., and Waldman, R.: Evaluation of CMIP6 DECK Experiments With CNRM-CM6-1, Journal of Advances in Modeling Earth Systems, 11, 2177–2213, https://doi.org/10.1029/2019MS001683, _eprint: https://onlinelibrary.wiley.com/doi/pdf/10.1029/2019MS001683, 890 2019.

von Lerber, A., Mech, M., Rinke, A., Zhang, D., Lauer, M., Radovan, A., Gorodetskaya, I., and Crewell, S.: Evaluating seasonal and regional distribution of snowfall in regional climate model simulations in the Arctic, Atmospheric Chemistry and Physics, 22, 7287–7317, https://doi.org/10.5194/acp-22-7287-2022, publisher: Copernicus GmbH, 2022.

Wang, C., Graham, R. M., Wang, K., Gerland, S., and Granskog, M. A.: Comparison of ERA5 and ERA-Interim near-surface air tempera-895 ture, snowfall and precipitation over Arctic sea ice: effects on sea ice thermodynamics and evolution, The Cryosphere, 13, 1661–1679, https://doi.org/10.5194/tc-13-1661-2019, publisher: Copernicus GmbH, 2019.

Wang, Z. and Sassen, K.: Level 2 Cloud Scenario Classification Product Process Description and Interface Control Document, Tech. rep., A NASA Earth System Science Pathfinder Mission, 2019.

Warren, S. G., Hahn, C. J., London, J., Chervin, R. M., Jenne, R. L. W. U., Colorado Univ., B., Colorado Univ., B., and National Center for 900 Atmospheric Research, B.: Global distribution of total cloud cover and cloud type amounts over the ocean, Tech. Rep. DOE/ER-0406; NCAR/TN-317-STR, USDOE Office of Energy Research, Washington, DC (USA). Carbon Dioxide Research Div.; National Center for Atmospheric Research, Boulder, CO (USA), https://doi.org/10.2172/5415329, 1988.

Wegener, A.: Thermodynamik der Atmosphäre, Nature, 90, 31–31, https://doi.org/10.1038/090031a0, number: 2237 Publisher: Nature Publishing Group, 1912.

905 Winker, D. M., Hunt, W. H., and McGill, M. J.: Initial performance assessment of CALIOP, Geophysical Research Letters, 34, https://doi.org/10.1029/2007GL030135, _eprint: https://onlinelibrary.wiley.com/doi/pdf/10.1029/2007GL030135, 2007.

Winker, D. M., Pelon, J., Coakley, J. A., Ackerman, S. A., Charlson, R. J., Colarco, P. R., Flamant, P., Fu, Q., Hoff, R. M., Kittaka, C., Kubar, T. L., Treut, H. L., Mccormick, M. P., Mégie, G., Poole, L., Powell, K., Trepte, C., Vaughan, M. A., and Wielicki, B. A.: The CALIPSO Mission: A Global 3D View of Aerosols and Clouds, Bulletin of the American Meteorological Society, 91, 1211–1230, 910 https://doi.org/10.1175/2010BAMS3009.1, publisher: American Meteorological Society Section: Bulletin of the American Meteorological Society, 2010.

Wood, N. B. and L'Ecuyer, T.: Level 2C Snow Profile Process Description and Interface Control Document, Product Version P1 R0, https://www.cloudsat.cira.colostate.edu/cloudsat-static/info/dl/2c-snow-profile/2C-SNOW-PROFILE_PDICD.P1_R05.rev0_.pdf, 2018.

Wood, N. B., L'Ecuyer, T. S., Heymsfield, A. J., Stephens, G. L., Hudak, D. R., and Rodriguez, P.: Estimating snow microphysical properties 915 using collocated multisensor observations, J. Geophys. Res. Atmos., 119, 8941–8961, https://doi.org/10.1002/2013JD021303, 2014.

Young, G., Connolly, P. J., Jones, H. M., and Choularton, T. W.: Microphysical sensitivity of coupled springtime Arctic stratocumulus to modelled primary ice over the ice pack, marginal ice, and ocean, Atmos. Chem. Phys., 17, 4209–4227, https://doi.org/10.5194/acp-17-4209-2017, 2017.

Zelinka, M. D., Myers, T. A., McCoy, D. T., Po-Chedley, S., Caldwell, P. M., Ceppi, P., Klein, S. A., and Taylor, K. E.: Causes of Higher Climate Sensitivity in CMIP6 Models, Geophysical Research Letters, 47, e2019GL085 782, https://doi.org/10.1029/2019GL085782, _eprint: https://agupubs.onlinelibrary.wiley.com/doi/pdf/10.1029/2019GL085782, 2020.

Zhang, D., Wang, Z., and Liu, D.: A global view of midlevel liquid-layer topped stratiform cloud distribution and phase partition from CALIPSO and CloudSat measurements, Journal of Geophysical Research: Atmospheres, 115, https://doi.org/10.1029/2009JD012143, _eprint: https://onlinelibrary.wiley.com/doi/pdf/10.1029/2009JD012143, 2010.

Zhang, T.: Influence of the seasonal snow cover on the ground thermal regime: An overview, Reviews of Geophysics, 43, https://doi.org/10.1029/2004RG000157, _eprint: https://onlinelibrary.wiley.com/doi/pdf/10.1029/2004RG000157, 2005.